nature aging

ARTICLES

https://doi.org/10.1038/s43587-021-00054-2

Hypoxia compromises the mitochondrial metabolism of Alzheimer's disease microglia via HIF1

Rosana March-Diaz[1,13], Nieves Lara-Ureña[1,13], Carmen Romero-Molina[1,2,3,13], Antonio Heras-Garvin[1,9,13], Clara Ortega-de San Luis[1,10,13], Maria I. Alvarez-Vergara[1], Manuel A. Sanchez-Garcia[1,11], Elisabeth Sanchez-Mejias[2,4,5], Jose C. Davila[2,4,5], Alicia E. Rosales-Nieves[1], Cristina Forja[1], Victoria Navarro[1,2,3], Angela Gomez-Arboledas[2,4,5], Maria V. Sanchez-Mico[1,2,3], Adrian Viehweger[1,12], Almudena Gerpe[6], Emma J. Hodson[7], Marisa Vizuete[1,2,3], Tammie Bishop[7], Alberto Serrano-Pozo[8], Jose Lopez-Barneo[1,2], Edurne Berra[6], Antonia Gutierrez[2,4,5], Javier Vitorica[1,2,3,14] ✉ and Alberto Pascual[1,14] ✉

Genetic Alzheimer's disease (AD) risk factors associate with reduced defensive amyloid β plaque-associated microglia (AβAM), but the contribution of modifiable AD risk factors to microglial dysfunction is unknown. In AD mouse models, we observe concomitant activation of the hypoxia-inducible factor 1 (HIF1) pathway and transcription of mitochondrial-related genes in AβAM, and elongation of mitochondria, a cellular response to maintain aerobic respiration under low nutrient and oxygen conditions. Overactivation of HIF1 induces microglial quiescence in cellulo, with lower mitochondrial respiration and proliferation. In vivo, overstabilization of HIF1, either genetically or by exposure to systemic hypoxia, reduces AβAM clustering and proliferation and increases Aβ neuropathology. In the human AD hippocampus, upregulation of HIF1α and HIF1 target genes correlates with reduced Aβ plaque microglial coverage and an increase of Aβ plaque-associated neuropathology. Thus, hypoxia (a modifiable AD risk factor) hijacks microglial mitochondrial metabolism and converges with genetic susceptibility to cause AD microglial dysfunction.

In 1919, del Río-Hortega[1,2] grouped several morphologic entities of the central nervous system under the term microglia (see ref. [3] for a commented English translation), showing that microglia could adapt to changing environments by activating migration, proliferation, growth and phagocytosis.

In Alzheimer's disease (AD), microglia adapt their morphology and function to cluster and establish a protective barrier around senile plaques[4]. Increasing evidence implicates the decline of microglial defensive responses in the progression of the disease: (1) single-nucleotide polymorphisms in several genetic loci encoding proteins with known roles in innate immunity are associated with an increased risk of developing AD[5]; (2) functional studies of AD-related polymorphisms suggest that microglia play a protective role in AD, which is altered by these individual loss-of-function genetic variants[6]; and (3) postmortem studies in AD brains have reported that microglial cells acquire a dysfunctional phenotype[7], degenerate[8] and die by apoptosis[9], thereby contributing to the deposition of amyloid β (Aβ) and the development of plaque-associated dystrophic neurites[4,10–12].

Why do AD microglia become dysfunctional? Aβ activates a plethora of signaling pathways, which converge in a common microglial neurodegenerative phenotype (MGnD) observed in all of the disease-associated microglia (DAM)[13,14]. Loss of function of genetic AD risk factors, such as the triggering receptor expressed on myeloid cells 2 (TREM2) and apolipoprotein E, is associated with microglial dysfunction characterized by reduced clustering and survival around Aβ plaques[10,12,15,16]. Based on these data, it has been suggested that microglial activation may be required not only to protect against neurodegeneration but also to avoid a low-energy state induced by the disease[17].

Microglia are the brain cells able to survive closer to Aβ plaques[18], and upregulation of hypoxia-inducible factor 1 (HIF1)—the master regulator of oxygen homeostasis[19]—has been suggested in Aβ plaque-associated microglia (AβAM)[17,20], indicating local low

---

[1]Instituto de Biomedicina de Sevilla (IBiS), Hospital Universitario Virgen del Rocio/CSIC/Universidad de Sevilla, Seville, Spain. [2]Centro de Investigación Biomédica en Red sobre Enfermedades Neurodegenerativas (CIBERNED), Madrid, Spain. [3]Departamento de Bioquimica y Biologia Molecular, Facultad de Farmacia, Universidad de Sevilla, Seville, Spain. [4]Departamento Biologia Celular, Genetica y Fisiologia, Facultad de Ciencias, Universidad de Málaga, Malaga, Spain. [5]Instituto de Investigación Biomédica de Málaga (IBIMA), Universidad de Málaga, Málaga, Spain. [6]CIC bioGUNE, Basque Research and Technology Alliance (BRTA), Derio, Spain. [7]Target Discovery Institute, Oxford, UK. [8]Department of Neurology, Massachusetts General Hospital, Harvard Medical School, Boston, MA, USA. [9]Present address: Division of Neurobiology, Department of Neurology, Medical University of Innsbruck, Innsbruck, Austria. [10]Present address: School of Biochemistry and Immunology, Trinity College Institute for Neuroscience, Trinity College Dublin, Dublin, Ireland. [11]Present address: Medical Research Council Centre for Inflammation Research, The Queen's Medical Research Institute, The University of Edinburgh, Edinburgh, UK. [12]Present address: Department of Pediatric Radiology, University Clinic Leipzig, Leipzig, Germany. [13]These authors contributed equally: Rosana March-Diaz, Nieves Lara-Ureña, Carmen Romero-Molina, Antonio Heras-Garvin, Clara Ortega-de San Luis. [14]These authors jointly supervised this work: Javier Vitorica, Alberto Pascual. ✉e-mail: vitorica@us.es; apascual-ibis@us.es

oxygen levels. In addition to nonmodifiable genetic risks, there are also potentially modifiable AD risk factors that together strongly contribute to the onset of dementia[21,22], by accelerating progression of the disease through multiple mechanisms. Several of these factors (for example, hypertension, obesity, atrial fibrillation, diabetes mellitus, physical inactivity and smoking) converge in altering the vascular system and/or reducing oxygen/nutrient availability[21–23]. We hypothesize that local clues synergize with systemic diseases progressing with hypoxia to activate HIF1 and compromise microglial function.

Results

The HIF1-mediated stress response pathway is induced in AβAM. It is suspected that the messenger RNA (mRNA) levels of *Hif1a* and several HIF1 targets, including those involved in anaerobic glycolysis (glucose to lactate), are upregulated in DAM[17,20]. The switch from aerobic respiration to anaerobic glycolysis has been proposed as a metabolic adaptation to sustain DAM energy demand[24], but also a detrimental event[20]. Therefore, we investigated the contribution of HIF1 to AβAM transcription. First, we showed that *Hif1a* mRNA is expressed around Aβ plaques in an AD mouse model (Fig. 1a). We then combined in situ hybridization (ISH) with immunofluorescence for the microglial ionized calcium-binding adaptor molecule 1 (IBA1) and revealed that AβAM also expressed high *Hif1a* mRNA levels (Fig. 1a), whereas low expression levels were observed in microglia distal to Aβ deposits and from wild-type mice (Fig. 1a,b). To further investigate whether *Hif1a* mRNA upregulation has functional consequences over AβAM transcription, we used transcription factor enrichment analysis (TFEA.ChIP)[25]. We found that HIF1α and HIF2α were among the top proteins predicted as regulators of *APP-PSEN1*/+ microglial transcription (Fig. 1c and Supplementary Table 1), suggesting a preponderant role of HIF-mediated transcription in AβAM.

To formally demonstrate HIF1-dependent transcriptional activation in AβAM, we defined the HIF1/hypoxia-induced microglial module (HMM) using a transcriptomic analysis of primary microglial cell cultures exposed to hypoxia or normoxia (hypoxia: 1% O_2 for 6 h; normoxia: 21% O_2 for 6 h). First, we checked that our cultures were enriched in microglia using immunofluorescence (Extended Data Fig. 1a) and quantitative PCR with reverse transcription (RT–qPCR; Extended Data Fig. 1b), performed principal component analysis (Extended Data Fig. 1c), identified the differentially expressed genes (Fig. 1d and Supplementary Tables 2 and 3), validated the differentially expressed genes by qRT–PCR (Extended Data Fig. 1b) and demonstrated their regulation by HIF1 using inducible Cx3cr1-Cre::ERT2-mediated deletion of *Hif1a* in primary microglial cultures (Fig. 1e,f). We then studied the transcriptional profile of isolated microglia from two mouse models: (1) an Aβ plaque-depositing APP_{751}SL model (APP mice; residues 1–751 of human APP with the Swedish and London mutations); and (2) a nondepositing mouse model with knock-in of a single copy of human *MAPT* encoding a p.Pro301Ser substitution (TAU mice). To this end, we developed a protocol based on the sorting of CD11b$^+$/CD45$^+$ microglia into CLEC7a$^+$ (strongly expressed by DAM[14,26,27]) and CLEC7a$^-$ (homeostatic) subpopulations (see Extended Data Fig. 2a–e for the gating strategy employed). CLEC7a$^+$ microglia were increased in 12-month-old APP and end-stage TAU mice (pathologic state), but remained unaltered in age-matched wild-type or 3-month-old AD models (prepathologic state; Extended Data Fig. 2f). Global gene expression profile studies (Extended Data Fig. 2g and Supplementary Table 4) followed by gene set enrichment analysis (GSEA) revealed that pathologic-state APP microglia showed strong enrichment of the HMM (Fig. 1g) while the TAU model presented only mild induction (Extended Data Fig. 1e and Supplementary Table 5), despite similar MGnD[27] gene set (Supplementary Table 6) enrichment in both models (Fig. 1g, Extended Data Fig. 1e and Supplementary Table 5), indicating a similar degree of activation. Direct comparison of the differentially expressed genes between APP and TAU pathologic state microglia revealed the HMM as the most enriched gene set in APP (Extended Data Fig. 1f and Supplementary Table 5), although these two experimental models had similar global transcription profiles (Extended Data Fig. 2g and Supplementary Table 5).

Then, we investigated whether the HIF1 pathway was also upregulated in other DAM. We reanalyzed the global expression profile data of microglia isolated form other neurodegenerative or aging models using CD45/CD11b markers[28–30]. Expectedly, the MGnD gene set was activated in microglia from all models (Extended Data Fig. 1g and Supplementary Table 7), whereas the HMM was a prominent characteristic of AβAM (Extended Data Fig. 1h and Supplementary Table 7) and was found to be only modestly upregulated in other DAM (Supplementary Table 7), suggesting that AβAM may be metabolically challenged by low oxygen levels.

Increased oxidative phosphorylation (OXPHOS)-related transcription in AD microglia. HIF1-mediated transcriptional programming normally induces a metabolic switch from aerobic mitochondrial respiration to anaerobic glycolysis[19]. Paradoxically, the OXPHOS gene set was dramatically enriched in both APP and TAU neurodegenerative mouse models (Fig. 2a, Extended Data Fig. 3a and Supplementary Tables 5 and 7), including upregulation of the mRNA levels of genes encoding proteins for all of the mitochondrial electron transport chain complexes (complexes I–IV) and complex V (ATPase) (Fig. 2a and Extended Data Fig. 3a). These data were confirmed by the enrichment of other gene sets implicated in aerobic respiration and ATP production (Fig. 2b). Moreover, gene sets related to antiviral responses and aerobic respiration represented around 50% of the top gene sets enriched in DAM (Extended Data Fig. 3b and Supplementary Table 5). Finally, we verified that the OXPHOS gene set was enriched in DAM from all of the neurodegenerative models and, somehow surprisingly, substantially reduced in the microglia from aged mice (Extended Data Fig. 3c and Supplementary Table 7).

To corroborate that our results were also relevant for human disease, we interrogated the data from a recent human single-cell RNA sequencing study[31]. Microglia isolated from postmortem human AD samples clustered in two groups differentiated from control microglia (Fig. 2c), and the genes encoding OXPHOS were significantly overexpressed in microglial cells from AD samples (Fig. 2c).

OXPHOS upregulation constitutes a bone fide indicator of mechanistic/mammalian target of rapamycin (mTOR) biosynthetic activity via mitochondrial activation[32], a pathway that has been described as regulated by TREM2 (ref. [17]). Interestingly, we reanalyzed the data from ref. [17] and observed that TREM2 deficiency is indeed associated with dramatic downregulation of the OXPHOS gene set in microglia from the *5xfAD*/+ mouse model (Fig. 2d and Supplementary Table 9), suggesting that TREM2 activates OXPHOS transcription in AβAM. Induction of protein synthesis, another mTOR activation landmark[33], was highly enriched in AβAM (Extended Data Fig. 3b and Supplementary Table 5). Thus, we also interrogated our transcriptomic data for the presence of an mTOR signature[17] (Supplementary Table 8) and found modest enrichment in both the Aβ and TAU models (Extended Data Fig. 3d).

Altogether, these data strongly indicate that an increase in transcription of the aerobic respiration-related genes takes place, both in AD mouse models and human AD microglia in a TREM2-dependent manner.

AβAM mitochondria are characterized by elongation. We have demonstrated that AβAM are characterized by simultaneous activation of two antagonistic pathways: (1) the HIF1 pathway (a classical trigger of anaerobic glycolysis[19]) (Fig. 1 and Extended Data Fig. 1);

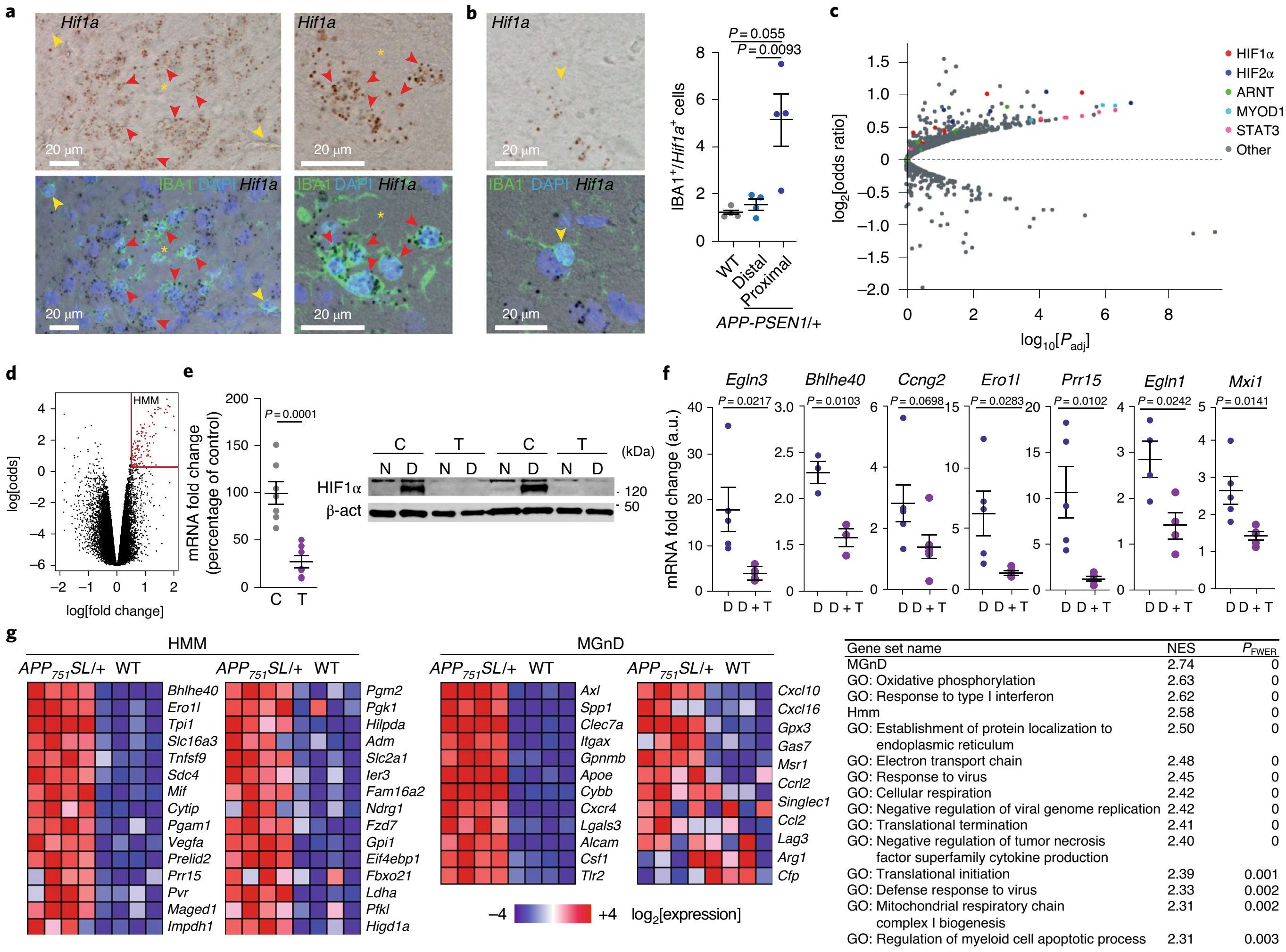

Gene set name	NES	P_{FWER}
MGnD	2.74	0
GO: Oxidative phosphorylation	2.63	0
GO: Response to type I interferon	2.62	0
Hmm	2.58	0
GO: Establishment of protein localization to endoplasmic reticulum	2.50	0
GO: Electron transport chain	2.48	0
GO: Response to virus	2.45	0
GO: Cellular respiration	2.42	0
GO: Negative regulation of viral genome replication	2.42	0
GO: Translational termination	2.41	0
GO: Negative regulation of tumor necrosis factor superfamily cytokine production	2.40	0
GO: Translational initiation	2.39	0.001
GO: Defense response to virus	2.33	0.002
GO: Mitochondrial respiratory chain complex I biogenesis	2.31	0.002
GO: Regulation of myeloid cell apoptotic process	2.31	0.003

Fig. 1 | HIF1-mediated transcription is activated in AβAM. a,**b**, ISH of *Hif1a* mRNA (brown) and immunohistochemistry for microglia (IBA1; green) and nuclear (DAPI; blue) staining in brain sections of 8-month-old *APP-PSEN1/+* mice (**a**) and WT mice (**b**) proximal (red arrowheads) and distal (yellow arrowheads) to Aβ plaques (yellow asterisks in **a**). Right in **b**: microglial quantification of IBA1+/*Hif1a*+ cells in the wild type (WT) and in regions distal and proximal to Aβ plaques ($n = 4$ mice; ANOVA with post-hoc Tukey's test). **c**, Transcription factor enrichment analysis of *APP-PSEN1/+* microglial transcription[25]. Each dot in the volcano plot represents an individual chromatin immunoprecipitation sequencing experiment. **d**, Volcano plot showing the genes included in the HMM (red dots; $P < 0.01$; log[fold change] > 0.5). **e**, Primary microglial cell cultures from *Cx3cr1-Cre::ERT2*; *Hif1a*$^{fl/fl}$ mice were treated with either vehicle (C) or tamoxifen (T) (100 nM; 6 d), and the effect on HIF1α expression was assayed by qRT-PCR (left; $n = 7$; Student's *t*-test) and western blot (right) in normoxia (N; 21% O_2; 24 h) and after DMOG (D; 0.1 mM; 24 h) treatment. **f**, Primary microglial cell cultures from *Cx3cr1-Cre::ERT2*; *Hif1a*$^{fl/fl}$ mice were treated with either vehicle, D, T or D plus T. The mRNA fold changes in D versus vehicle (D) and D plus T versus T (D + T) are represented. *Hmbs* levels were used as housekeeping controls ($n = 5$ for *Egln3*, *Ero1l*, *Prr15* and *Mxi1*; $n = 3$ for *Bhlhe40*; $n = 6$ for *Ccng2*; $n = 4$ for *Egln1*; two-sided Student's *t*-test). **g**, GSEA of APP DAM versus wild-type 12-month-old microglia. The heat maps show the top-30-ranking genes of the HMM (left) and MGnD (right) gene sets. Red symbolizes overexpression and blue represents downregulation. Right: table of the 15 top gene sets, enriched in the APP pathologic state versus wild-type microglia, with a family-wise error rate *P* value (P_{FWER}) of <0.05. NES, normalized enrichment score. All data are presented as means ± s.e.m. *n* values represent the number of biologically independent experiments.

and (2) aerobic respiration (Fig. 2 and Extended Data Fig. 3). We have also shown that the HIF1 pathway is particularly enriched in AβAM versus other DAM (Fig. 1 and Extended Data Fig. 1). This peculiar metabolic adaptation of AβAM suggests that mitochondrial activity is essential for microglial metabolic fitness in response to Aβ and that HIF1 activation could be an unwanted byproduct of the chronic defensive activity of innate immune cell clusters (only present in Aβ-depositing mouse models). In addition, a reduction of the vasculature around Aβ plaques has been reported consistently in the literature in both the human AD brain and AD mouse models[23,34], which could also contribute to the high HIF1 activation. To better understand this paradoxical situation, we searched for situations where mitochondrial activity is preserved despite HIF1 activation and found that cells under nutrient and oxygen deprivation prevent a HIF1-mediated switch to anaerobic glycolysis by elongating mitochondria[35]—a well-described process that optimizes aerobic ATP production and prevents mitophagy[36]. Therefore, we first evaluated mitochondrial levels by immunofluorescence and observed clear upregulation of NDUFS2 complex I protein in AβAM compared with wild-type microglia or those distal to Aβ plaques (Fig. 3a). As AβAM phagocytize other cells and are in close apposition with dystrophic neurites that also contain mitochondria, we investigated the morphology of AβAM mitochondria using electron microscopy. Microglia distant from Aβ plaques presented round-shaped mitochondria (Fig. 3b), but AβAM showed elongated mitochondria surrounded by rough endoplasmic reticulum (Fig. 3c; characterized by

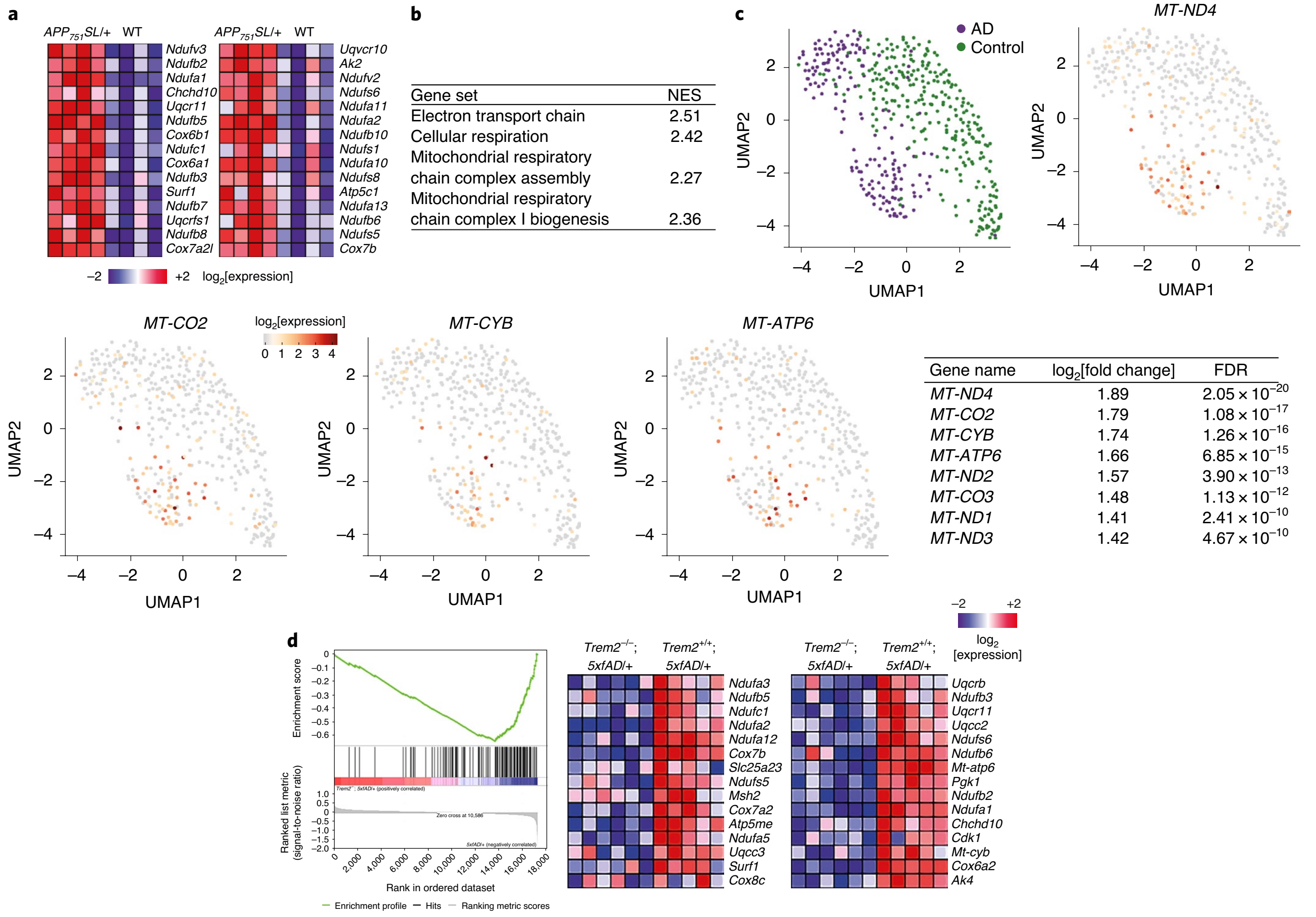

Gene set	NES
Electron transport chain	2.51
Cellular respiration	2.42
Mitochondrial respiratory chain complex assembly	2.27
Mitochondrial respiratory chain complex I biogenesis	2.36

Gene name	$\log_2$[fold change]	FDR
MT-ND4	1.89	2.05×10^{-20}
MT-CO2	1.79	1.08×10^{-17}
MT-CYB	1.74	1.26×10^{-16}
MT-ATP6	1.66	6.85×10^{-15}
MT-ND2	1.57	3.90×10^{-13}
MT-CO3	1.48	1.13×10^{-12}
MT-ND1	1.41	2.41×10^{-10}
MT-ND3	1.42	4.67×10^{-10}

Fig. 2 | AD microglia increase aerobic respiration-related transcription. a, GSEA of APP DAM versus wild-type 12-month-old microglia. The heat maps show the top-30-ranking leading-edge genes of the OXPHOS gene set. Red symbolizes overexpression and blue represents downregulation. **b**, Aerobic respiration-related gene sets enriched in APP DAM versus wild-type microglia (false discovery rate *q* value = 0). **c**, Single-nuclei RNA sequencing of human entorhinal cortex (http://adsn.ddnetbio.com/; ref. [31]). Top row (left): uniform manifold approximation and projection visualization of microglial cells from AD and control samples. Top row (right) and bottom row: relative gene expression (color intensity; see scale bar) of four representative OXPHOS genes. The table (right) includes the changes in expression ($\log_2$[fold change] and false discovery rate (FDR) *q* values) of the OXPHOS genes between AD and control microglial cells. **d**, Enrichment plot (left) and heat maps (right) of the oxidative OXPHOS gene set in *Trem2*$^{-/-}$; *5xfAD/+* versus *5xfAD/+* microglia.

an increased perimeter and aspect ratio) and decreased circularity versus wild-type microglia or those distal to Aβ plaques (Fig. 3d).

Altogether, these results indicate that aerobic respiration is a common feature of neurodegenerative DAM, while the concomitant activation of HIF1-mediated gene expression and elongation of their mitochondria suggest that AβAM metabolism is compromised.

Overactivation of HIF1 induces microglial quiescence. To verify that activation of microglia depends on mitochondrial activity, we treated microglial cell primary cultures with oligomeric Aβ (oAβ) for 24 h and measured the mitochondrial O_2 consumption rate. Interestingly, 24 h after stimulation, clear upregulation of the mitochondrial maximal respiratory capacity was observed (Fig. 4a). This was accompanied by a slight but significant increase in the mitochondrial protein SDHA (complex II), a trend for NDUFS2 to increase (complex I; Fig. 4b) and no changes in ATPsynβ (complex V; Fig. 4b). oAβ also induced the microglial response characterized by an increase of *Tnf* and *Il6* mRNA levels (Fig. 4c). Altogether, our data indicate that, in vitro, mitochondrial activity is upregulated by oAβ treatment; however, the magnitude of the activation was smaller than in vivo, probably due to the rich medium used in culture. To investigate whether a reduction of mitochondrial activity by exacerbation of the HIF1 response could compromise microglial responses to Aβ, we exposed normoxic and hypoxic microglial cell primary cultures to oAβ for 24 h. Interestingly, hypoxia reduced the basal levels of *Tnf* and *Il6* mRNA and blunted the normoxic response to oAβ (Fig. 4c). The reduction in microglial response was similar to that observed in primary microglial cell cultures from *Trem2*$^{-/-}$ mice exposed to 3 h of oAβ (Fig. 4c).

To further characterize the role of hypoxia in microglial cells, we first reanalyzed the transcriptomic data obtained from the primary microglial cells exposed to low oxygen levels (1% O_2 for 6 h; Fig. 1d and Extended Data Fig. 1a). As expected, hypoxia induced a robust transcriptional response characterized by coordinated induction of glycolytic genes (Fig. 4d, Extended Data Fig. 4a and Supplementary Table 10). Correspondingly, the glycolytic rate showed a clear increase in primary microglial cells exposed to hypoxia (Fig. 4e). In parallel, low oxygen levels repressed mitochondrial OXPHOS, as shown by GSEA and oxygen consumption recordings in hypoxic primary microglial cultures (Fig. 4f–g, Extended Data Fig. 4b and Supplementary Table 10). Consequently, in cellulo hypoxia induced a significant decrease in the ratio between mitochondrial oxygen consumption and glycolytic proton efflux rates (PERs) in microglia (Fig. 4h). Interestingly, the upregulation of anaerobic glycolysis

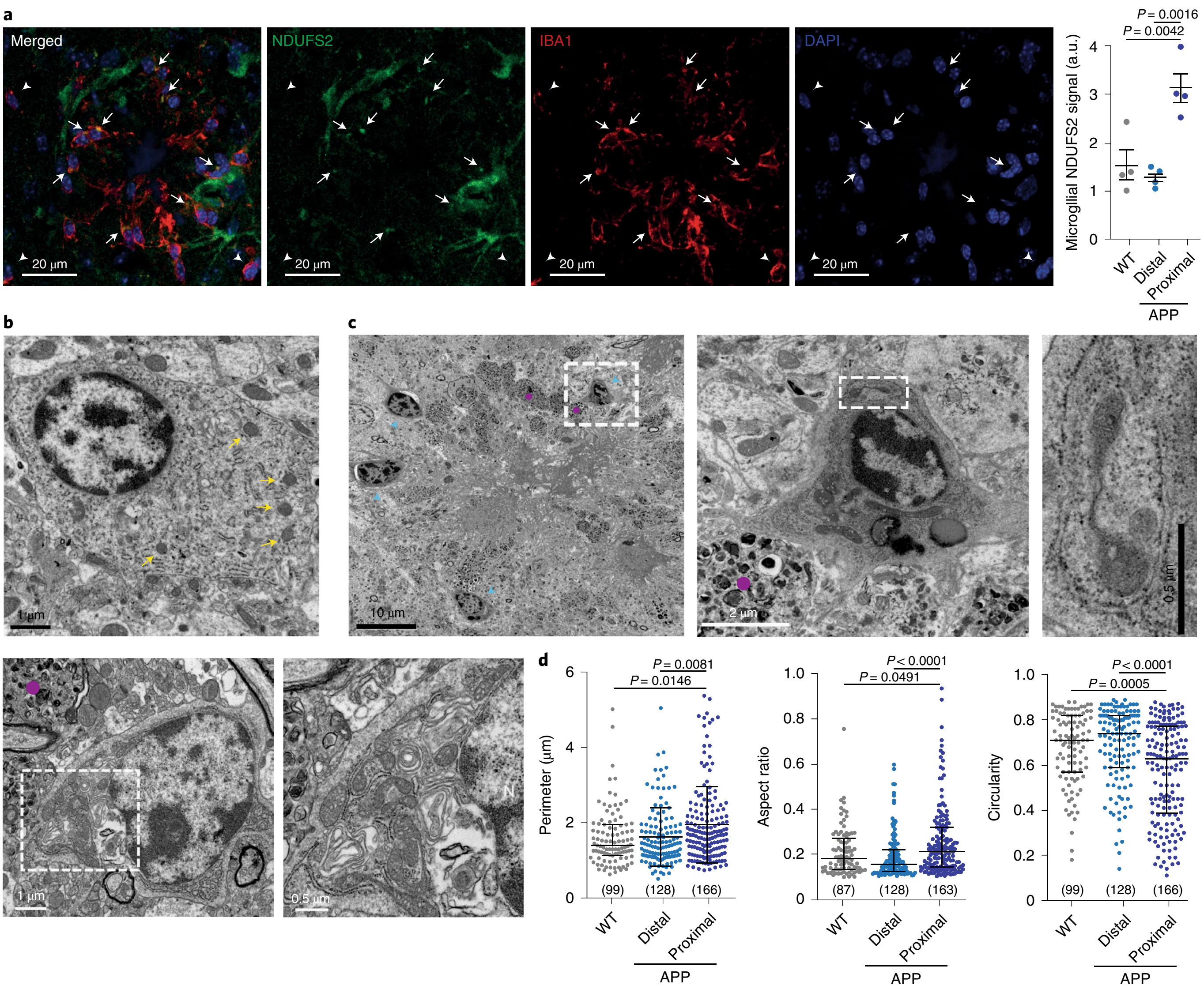

Fig. 3 | Mitochondria are elongated in an AD mouse model. a, Left: cortical confocal *xy* images from 8-month-old *APP-PSEN1/+* mice stained with mitochondrial complex I (NDUFS2; green), microglia (IBA1; red) and nuclear markers (DAPI; blue). The arrows and arrowheads indicate proximal and distal microglia, respectively. Right: quantification of the microglial (IBA1$^+$) NDUFS2 signal in wild-type mice and in areas distal and proximal to Aβ plaques ($n = 4$ mice; ANOVA with post-hoc Tukey's test). **b**,**c**, Electron microscopy images of hippocampal brain sections distal (**b**) and proximal (**c**) to Aβ plaques in pathologic-state *APP-PSEN1/+* mice. Microglia can be recognized by their darker cytoplasm and mitochondria by their morphology. Mitochondria are highlighted with yellow arrows. Some dystrophic neurites are labeled with pink circles as indicators of Aβ proximity. Blue arrowheads indicate microglial cells. In image in **c** is a magnification of the area indicated by the white box in the image to the left on the same row. The top right image in **c** has been rotated by 90° compared with the original image. **d**, Quantification of the perimeter, aspect ratio and circularity of mitochondria from wild-type microglial cells and microglia distal and proximal to Aβ plaques. The numbers of cells are indicated in parentheses (data from four wild-type and three *APP-PSEN1/+* mice; Mann–Whitney *U*-test with post-hoc Dunn's test). All data are presented as means ± s.e.m. *n* values represent the number of biologically independent experiments.

(Fig. 4d,e and Extended Data Fig. 4c,d) was accompanied by drastic downregulation of the overall cellular function, including DNA replication, suggesting that slowdown of mitochondrial activity may induce microglial quiescence (Extended Data Fig. 5a,b).

To evaluate whether hypoxia inhibited proliferation of microglia, we used two models: the microglial-derived BV2 cell line; and mouse primary microglial cell cultures. To determine whether hypoxia (1% O_2 for 4–48 h) modulates the BV2 cell cycle, we measured the percentage of cells in the G0/G1, S or G2 phase using propidium iodide staining and flow cytometry. Brief hypoxia (4 h) did not change the BV2 cell cycle; however, 24 and 48 h of hypoxia led to dramatic cell cycle arrest (Extended Data Fig. 6a). To differentiate between the induction of senescence (irreversible cell cycle arrest) or quiescence (reversible cell cycle arrest) by hypoxia, we exposed BV2 hypoxic cultures to 24 h of reoxygenation. Interestingly, the cell cycle was completely restored after incubation in normoxia (Extended Data Fig. 6b). To evaluate the involvement of HIF in control of the cell cycle under hypoxia, we interfered the expression of *Hif1a*, *Epas1* (encoding for HIF2α) or *Hif1a* and *Epas1*. Although the degree of suppression reached was small (around 50–60% of the levels of non-interfered cultures; Extended Data Fig. 6c), we were able to observe a decrease in hypoxia-induced cell cycle arrest when both genes were knocked down (Extended Data Fig. 6c). To confirm the role of HIF in hypoxia-mediated cell cycle arrest, we first exposed BV2 cells to dimethyloxalylglycine (DMOG)—an inhibitor of the main negative regulators of HIF stability, the prolyl-hydroxylases (PHDs)[19]—and observed a hypoxia-like cell cycle arrest in BV2 (Extended Data Fig. 6d). Second, we performed primary microglial cell cultures from either Egl9 homolog 2 (*Egln2*$^{-/-}$) (encoding for PHD1), *Egln1*$^{+/-}$ (PHD2; full PHD2 deficiency is not viable) or *Egln3*$^{-/-}$ mice (PHD3). The number of microglial cells was decreased both in the absence of PHD3 or in the presence of a half dose of PHD2 (Fig. 4i), whereas no differences were observed in PHD1-deficient microglia (Fig. 4i), further supporting a role for HIF in microglial proliferation[37,38]. Finally, we estimated proliferation in primary microglial cell cultures exposed to 24 h of hypoxia (1% O_2), using a bromodeoxyuridine (BrdU) incorporation assay. Hypoxia induced a notable decrease in BrdU$^+$ microglial cells (Fig. 4j). To confirm the role of HIF1 in microglial cell cycle arrest induced by hypoxia, we used primary microglial cell cultures with conditional deletion of *Hif1a* (Fig. 1e) exposed to hypoxia. As expected, hypoxia produced decrease in the number of BrdU$^+$ cells of a ~60%. However, microglial proliferation was almost completely restored in HIF1α-deficient cultures (Fig. 4k), demonstrating that HIF1 contributes to the reversible microglial cell cycle arrest under hypoxia.

A decrease of mitochondrial metabolism via HIF1 reduces AβAM. The formation of new Aβ plaques in APP-overexpressing mouse models is associated with microglia proliferation[18,39]. However, we have shown that, in cellulo, HIF1 overactivation induces microglial quiescence characterized by a low response to oAβ and reversible cell cycle arrest (Fig. 4). Therefore, we postulated that the proliferation (and therefore the clustering) of microglia around Aβ plaques in vivo depends on the balance between glycolysis and aerobic respiration.

In normoxia, *Hif* genes are constitutively transcribed and translated, but the resultant protein is degraded by the proteasome through oxygen-dependent hydroxylation by PHDs and von Hippel–Lindau (VHL)-mediated ubiquitination[19]. As overstabilization of HIF1 by VHL deficiency induces anaerobic glycolysis and inhibition of aerobic respiration[40], we created a new conditional AD mouse model with VHL depletion in adult microglia (*Cx3cr1-Cre::ERT2*; *Vhl*$^{fl/-}$; *APP-PSEN1*/+) (Fig. 5a). VHL deficiency induced the HMM in vivo, as demonstrated by global expression profile studies in isolated microglia (Fig. 5b and Supplementary Table 11) and a decrease in OXPHOS gene set transcription (Fig. 5c). Interestingly, this transcriptional regulation was associated with a decrease in the percentage of microglia, as observed by flow cytometry (Fig. 5d). Remarkably, VHL deficiency induced a decrease in the common microglial signature (MGnD gene set; Fig. 5e) in a transcriptional phenotype similar to TREM2 deficiency (for a review, see ref. [41]), suggesting reduced AβAM. Therefore, we quantified the IBA1 immunoreactivity around Aβ plaques and observed a decrease in the microglial coverage of cortical Aβ deposits in the absence of VHL (Fig. 5f). Altogether, these results indicate that downregulation of AβAM aerobic respiration by HIF1 stabilization induces a microglial dysfunctional phenotype similar to the one observed in TREM2 deficiency.

Several modifiable AD risk factors (for example, hypertension, obesity, atrial fibrillation, diabetes, physical inactivity and smoking) converge in altering the vascular system and/or reducing oxygen/nutrient availability[21,23]. We reasoned that these AD risk factors could contribute to the microglial dysfunction described in the human AD brain by disrupting the HIF1/aerobic respiration metabolic equilibrium observed in AβAM. To test this idea, we exposed 14-month-old wild-type or *APP-PSEN1*/+ mice to either normoxia (21% O_2) or sustained hypoxia (9% O_2) for 21 d and quantified IBA1$^+$ microglia in the hippocampus. We found a significant decrease in the number of IBA1$^+$ microglia in hypoxic *APP-PSEN1*/+ mice compared with normoxic *APP-PSEN1*/+ mice, whereas only a trend was detected in hypoxic compared with normoxic wild-type mice (Fig. 6a). Similarly, RT–qPCR in hippocampal extracts rendered significantly decreased levels of *Iba1* mRNA without changing *glial fibrillary acidic protein* (*Gfap*) astrocytic mRNA levels in *APP-PSEN1*/+ (Fig. 6b), and no differences were found in wild-type mice (Extended Data Fig. 7a). More strikingly, the distribution of microglia was altered by sustained hypoxia, showing an absence of clustering around Aβ plaques (Fig. 6a), suggesting a defect in AβAM. Closer examination of hippocampal and cortical regions of *APP-PSEN1*/+ mice revealed that hypoxic AβAM either did not invade the plaques or were simply absent (Fig. 6c)—a phenocopy of the microglial dysfunction observed in microglia deficient for VHL (Fig. 5f) and in TREM2-deficient mice[41]. This observation was confirmed using tomato lectin as an independent microglial marker (Fig. 6c). Quantification of both the IBA1$^+$ cell number and the area occupied by IBA1$^+$ staining per Thioflavin-S$^+$ (Thio-S$^+$) plaque demonstrated fewer AβAM in the hippocampus and cortex of hypoxic versus normoxic *APP-PSEN1*/+ mice (Fig. 6d).

Fig. 4 | Hypoxia induces cell cycle arrest via HIF1 in microglia in cellulo. a, Mitochondrial respiration OCR (left) and maximal respiration (right) of control (C) or oAβ-treated (10 µm; 24 h) mouse primary microglial cultures by Seahorse. Dashed lines indicate injection times ($n=3$ independent cultures; two-sided Student's *t*-test). FCCP, carbonyl cyanide-*p*-trifluoromethoxyphenylhydrazone. **b**, Protein levels of SDHA, NDUFS2 and ATPsynβ in cultures treated as in **a**. RPL26 was used as a housekeeping control (*n* values are indicated in parentheses; two-sided Student's *t*-test). **c**, *Tnf* and *Il6* mRNA levels in cultures treated as in **a** and exposed to normoxia (N; 21% O_2; 24 h) or hypoxia (H; 1% O_2; 24 h) (top), or from wild-type or *Trem2*$^{-/-}$ mice (bottom) (*n* values are indicated in parentheses; two-sided Student's *t*-test). a.u., arbitrary units. **d**,**f**, Heat maps of mouse primary microglial cultures exposed to hypoxia (6 h) versus normoxia. The top-30-ranking genes in two gene sets (KEGG glycolysis/gluconogenesis (**d**) and KEGG oxidative phosphorylation (**f**)) are shown. Red symbolizes overexpression and blue represents downregulation. **e**, ECAR (left) and basal PER (right) of mouse primary microglial cultures in exposed to hypoxia or normoxia (24 h) by Seahorse. ($n=5$ for normoxia; $n=6$ for hypoxia; two-sided Student's *t*-test). 2-DG, 2-deoxy-D-glucose. **g**, Mitochondrial respiration OCR (left) and basal respiration OCR (right) of mouse primary microglial cultures exposed to normoxia or hypoxia (24 h) by Seahorse. Discontinued lines show injection times ($n=5$ cultures for normoxia; $n=6$ cultures for hypoxia: two-sided Student's *t*-test). **h**, Mitochondrial respiration OCR (mytoOCR)/basal PER (glycoPER) ratio of mouse primary microglial cultures exposed to normoxia or hypoxia by Seahorse ($n=4$ for normoxia; $n=6$ for hypoxia; two-sided Student's *t*-test). **i**, Left: images of primary microglial cultures, stained with IBA1 (red) and GFAP (green) and counterstained with DAPI (blue), from wild-type (*Egln1*$^{+/+}$) or *Egln1*$^{+/-}$ mice. Right: graphs showing the percentage of microglia in each mutant (knockout (KO) or heterozygous (HET)) relative to their control (C). *n* values are indicated in parentheses (two-sided Student's *t*-test). **j**, Left: images of proliferation in primary microglial cultures (red) exposed to either normoxia, hypoxia or DMOG (D; 24 h; 0.1 mM) and incubated with 10 µM BrdU (3 h). Insets: magnified views of the areas highlighted by white dashed boxes. The white arrowheads point to BrdU$^+$/IBA1$^+$ cells and the yellow arrowhead indicates a BrdU$^+$/IBA1$^-$ cell. Right: graph showing quantification of the results ($n=4$; two-sided Student's *t*-test). **k**, Left: images of primary microglial cultures from *Cx3cr1-Cre::ERT2*; *Hif1a*$^{fl/fl}$ mice treated with either vehicle (C) or tamoxifen (T; 100 nM; 6 d). Arrowheads indicate BrdU-reactive microglial cells. Right: numbers of BrdU-reactive microglial cells exposed to hypoxia (24 h), presented as the percentage relative to those exposed to normoxia ($n=7$ for the control; $n=6$ for the tamoxifen treatment; two-sided Student's *t*-test). All data are presented as means ± s.e.m. *n* values represent the number of biologically independent experiments.

In sharp contrast, neither the number of reactive astrocytes (GFAP$^+$) nor the number of total astrocytes (glutamine synthetase (GluS$^+$)) was altered by sustained hypoxic treatment in *APP-PSEN1*/+ mice (Extended Data Fig. 7b). Moreover, the ratio of astrocytes adjacent to Aβ plaques (within 20 µm from the plaque edge) versus total astrocytes was not significantly different (Extended Data Fig. 7b,c). The sustained hypoxia treatment induced an expected increase in hematocrit (Extended Data Fig. 7d) and no infarctions were observed in the hypoxic brains of wild-type or *APP-PSEN1*/+ mice (Extended Data Fig. 7e). Finally, we showed that hypoxia reduced AβAM proliferation using Ki67 staining in the hippocampus and cortex of *APP-PSEN1*/+ mice (Fig. 6e); no changes were observed by hypoxic treatment in wild-type mice (Extended Data Fig. 7f).

Altogether, these results suggest that systemic comorbidities may contribute to brain hypoxia/hypoperfusion-induced microglial quiescence by disrupting the HIF1/aerobic respiration metabolic equilibrium in AβAM.

Sustained hypoxia enhances Aβ local pathology. Defects in microglial clustering around plaques by *TREM2* haploinsufficiency decreased Aβ plaque compaction[10,11], highlighting the protective barrier function of microglia around plaques[4]. We therefore asked whether the reduced clustering of microglia induced by sustained hypoxia correlated with an increase in Aβ levels in *APP-PSEN1*/+ mice. We observed an increase in both dense-core Thio-S$^+$ and total Aβ$^+$ plaque load and number in the cortex of hypoxic *APP-PSEN1*/+ mice (9% O_2) compared with normoxic (21% O_2) AD littermates (Fig. 7a–f), despite no significant differences in the total Aβ levels by enzyme-linked immunosorbent assay (ELISA), nor in the processing of APP[42]. As a control, we also showed that no Thio-S$^+$

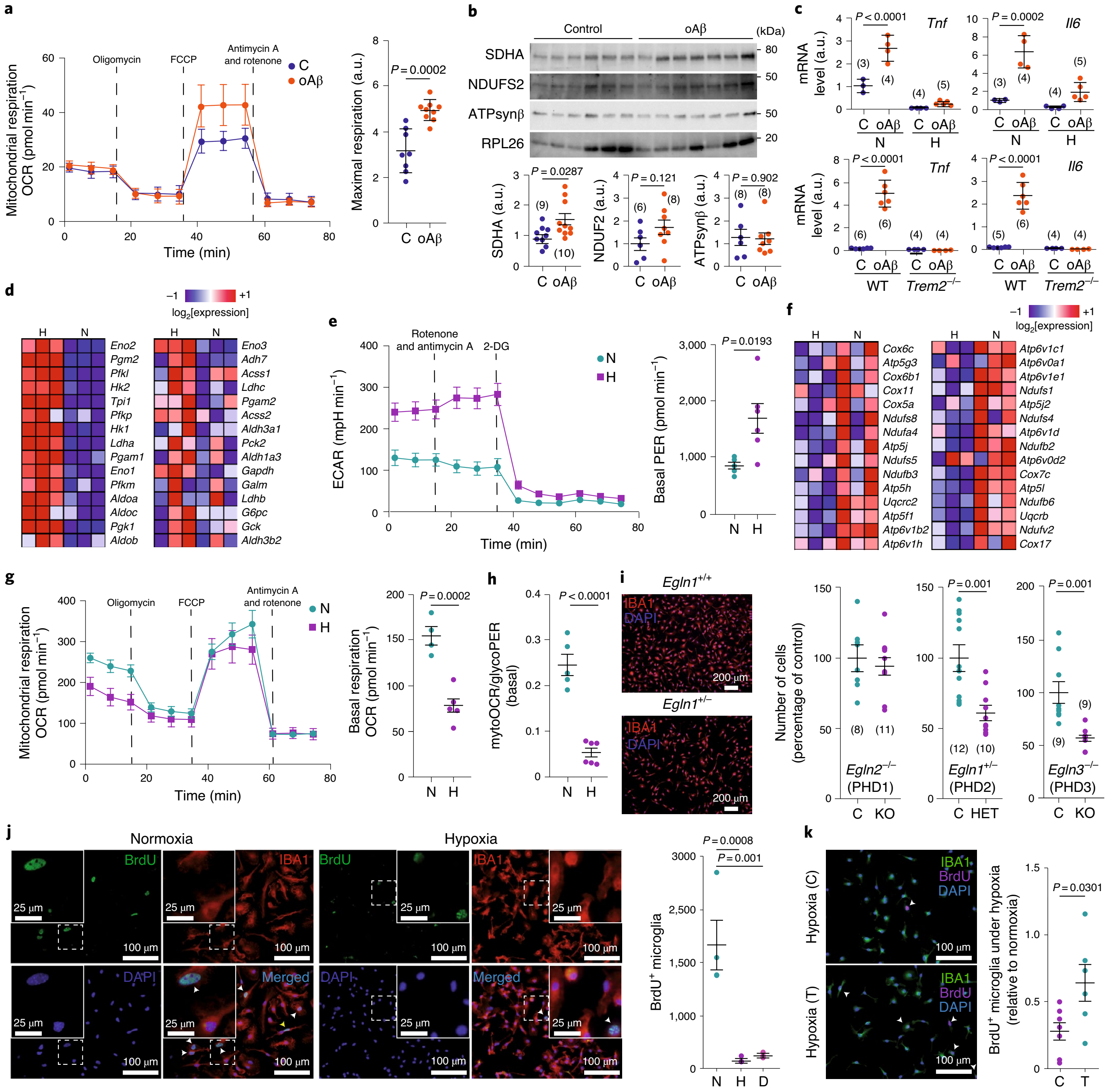

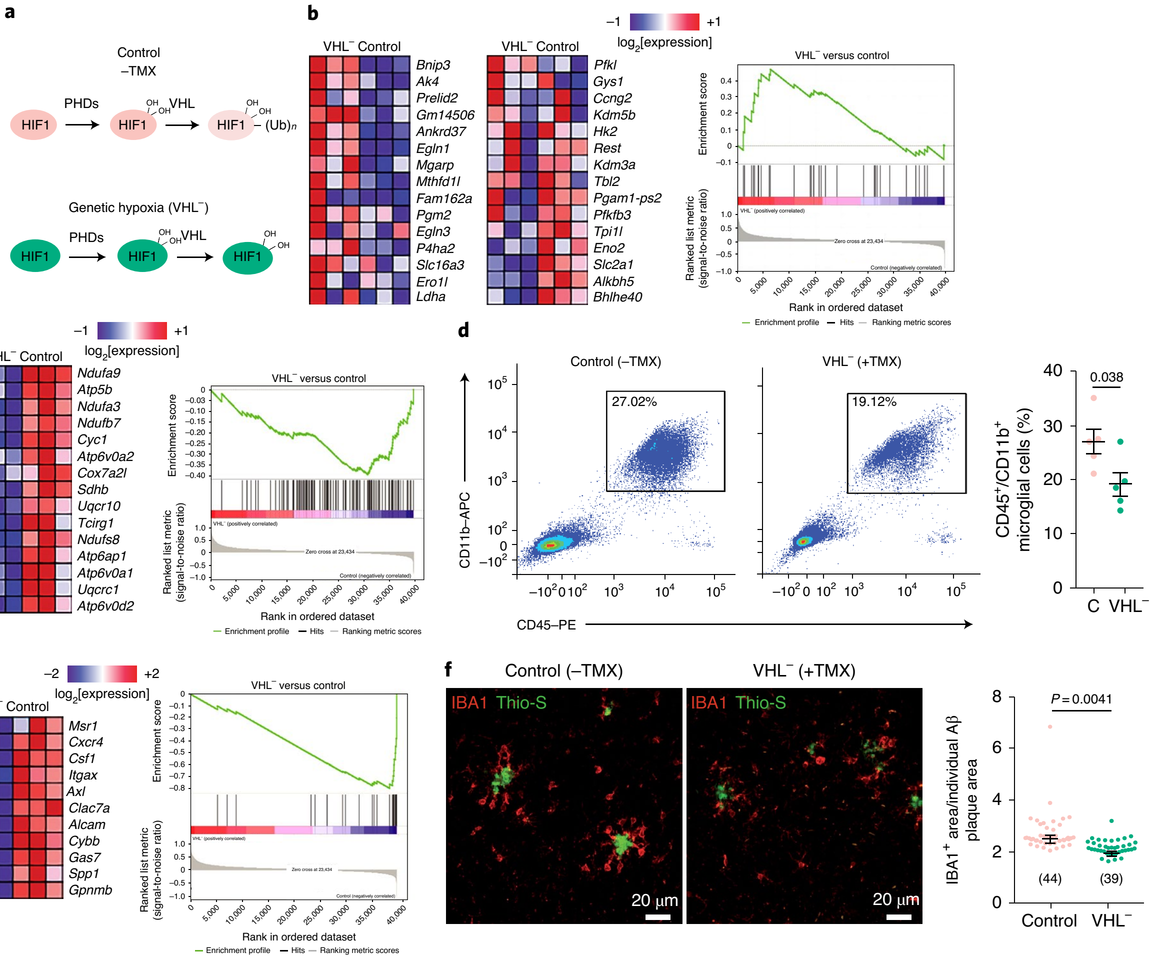

Fig. 5 | Overstabilization of HIF1 reduces AβAM in vivo. Analysis of microglia from *Cx3cr1-Cre::ERT2*; *APP-PSEN1/+*; *Vhl*$^{fl/-}$ mice untreated (control; –TMX) or treated (VHL⁻) with tamoxifen (30 d). **a**, Schematic of the mouse models used to generate genetic hypoxia (HIF overstabilization by VHL deletion) in adult microglia. **b**,**c**, GSEA. Heat maps and enrichment plots of the top-30-ranking leading-edge genes for the HMM (**b**) and OXPHOS (**c**) gene sets. Red symbolizes overexpression and blue represents downregulation. **d**, Left and middle: adult microglia isolated from control mice or mice treated (VHL⁻) with tamoxifen (30 d) using fluorescence-activated cell sorting. Right: quantification of the percentage of CD45$^+$/CD11b$^+$ cells in mice without (C) or with tamoxifen (VHL⁻) treatment ($n = 5$; two-sided Student's *t*-test). **e**, Heat map (left) and enrichment plot (right) of the MGnD gene set. **f**, Left: cortical sections stained with IBA1 (red) and Thio-S (green). Right: quantification of the percentage of the Aβ plaque area occupied by IBA1$^+$ microglia in control mice and those treated with tamoxifen (VHL⁻; 30 d). *n* values are indicated in parentheses (two-sided Student's *t*-test). All data are presented as means ± s.e.m. *n* values represent the number of biologically independent experiments.

(Extended Data Fig. 8a) or Aβ$^+$ (Extended Data Fig. 8b) plaques were found in normoxic or hypoxic wild-type mice. Furthermore, the size distribution of cortical Thio-S$^+$ and total Aβ$^+$ plaques in hypoxic and normoxic *APP-PSEN1/+* mice revealed enrichment in plaques under hypoxia, suggesting that low oxygen enhances Aβ aggregation, resulting in more newly formed plaques (Fig. 7c,f). Levels of soluble Aβ_{1-42} in normoxic and hypoxic *APP-PSEN1/+* mice, measured by ELISA, showed a trend to increase under hypoxia (Fig. 7g), and dot blots with a fibrillar Aβ oligomer-specific antibody (OC) showed a clear increase of OC immunoreactivity in cortical soluble extracts from hypoxic versus normoxic *APP-PSEN1/+* mice (Fig. 7h). Altogether, these data suggest that sustained hypoxia potentiates Aβ aggregation and deposition in brain parenchyma.

As the result of the direct neurotoxic effect of Aβ, dense-core (senile) plaques are decorated with dystrophic neurites, which can be displayed with both ubiquitin and phospho-TAU (p-TAU) immunohistochemistry. The AD-linked p.Arg47His and p.Arg62His TREM2 variants impair the microglial barrier function and worsen plaque-associated axonal dystrophies[10–12]. Therefore, we investigated whether sustained hypoxia could aggravate this neurodegenerative feature in an AD mouse model. *APP-PSEN1/+* mice exposed to sustained hypoxia showed a trend for increased ubiquitin load (Fig. 7i) and clear augmentation in the density of p-TAU$^+$ dystrophic neurites per Thio-S$^+$ plaque (Fig. 7j). As expected, we also showed that no p-TAU$^+$ dystrophic neurites (Extended Data Fig. 8c) were found in normoxic or hypoxic wild-type mice. We have previously shown that hippocampal somatostatin and neuropeptide Y interneurons are particularly vulnerable and die at early stages in a similar AD mouse model[43]. Here, we detected a significant further decrease in the mRNA levels of both somatostatin (*Sst*) and neuropeptide Y (*Npy*) under sustained hypoxic stress (Fig. 7k). Thus, these data indicate that sustained hypoxia leads to an increase in soluble Aβ fibrillar oligomers and newly formed dense-core Aβ plaques, and aggravates Aβ plaque-associated neurodegenerative phenomena.

Nude Aβ plaques with high pathology in hypoxic brain areas. To study the contribution of HIF1 induction in the AD human brain, we first reanalyzed the data of an RNA sequencing study of isolated cell types from the human brain[44]. Interestingly, the *HIF1a*

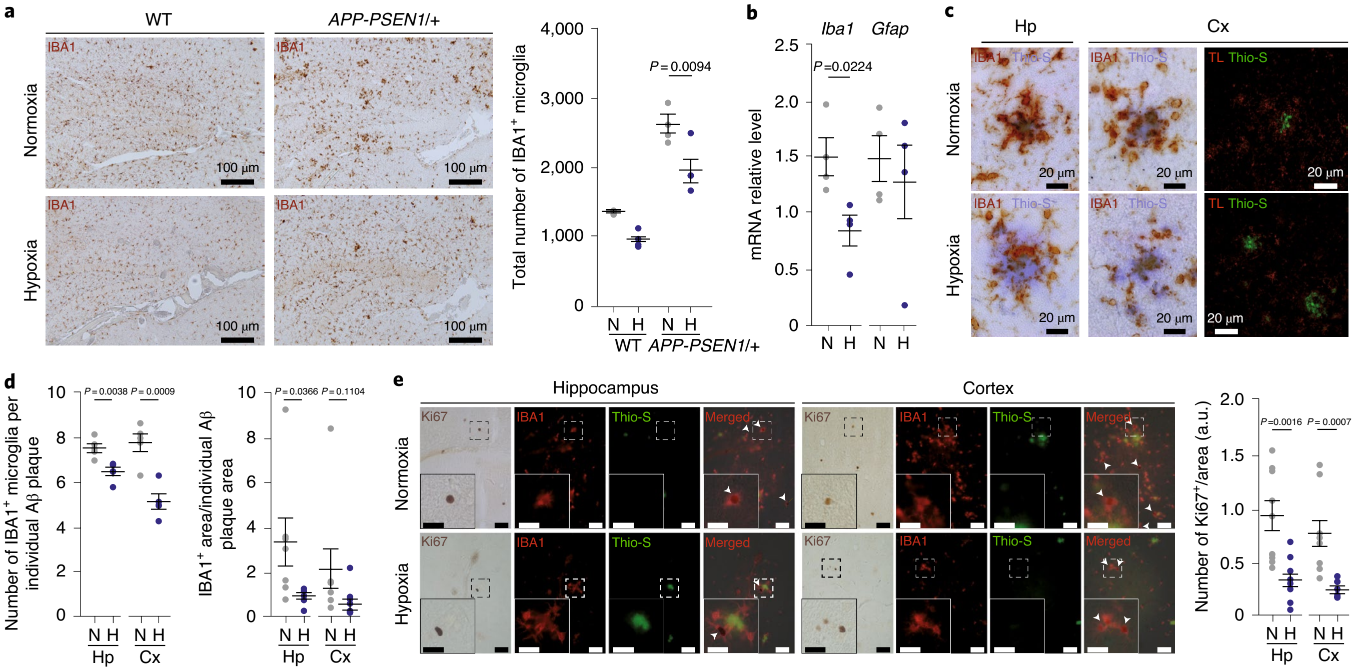

Fig. 6 | Systemic sustained hypoxia decreases clustering of AβAM. a–e, Left: 14-month-old wild-type and *APP-PSEN1/+* (AD) mice exposed to normoxia (N; 21% O_2) or sustained hypoxia (H; 9% O_2) for 21 d were studied. **a**, Hippocampal brain slices stained for IBA1. Right: quantification of the total number of IBA1⁺ microglia ($n = 3$ for the wild type exposed to normoxia; $n = 4$ for all other groups; two-sided Student's *t*-test). **b**, Relative levels of *Iba1* and *Gfap* mRNA in the hippocampus of *APP-PSEN1/+* mice exposed to hypoxia and normoxia. *Gapdh* mRNA was used as a housekeeping control ($n = 4$ mice per group; two-sided Student's *t*-test). **c**, Hippocampal (Hp; left) and cortical (Cx; right) sections stained with IBA1 (brown) and Thio-S (lilac) or tomato lectin (TL; red) and Thio-S (green). **d**, Quantification of the number of IBA1⁺ microglial cells per Aβ plaque (left; $n = 5$ mice; two-sided Student's *t*-test) and the percentage of the area of individual Aβ plaque occupied by IBA1⁺ microglia (right; $n = 7$ for Hp/N; $n = 8$ for Hp/H and Cx/N; $n = 9$ for Cx/H; two-sided Student's *t*-test). **e**, Left: representative images of hippocampal (left) and cortical (right) sections stained for Ki67 (brown; phase contrast) and IBA1 (red) and counterstained with Thio-S (green). The arrowheads indicate Ki67⁺ microglia. Insets: magnified images of the areas highlighted by white dashed boxes. Scale bars, 50 μm (main images) and 25 μm (insets). Right: quantification of the density of Ki67⁺ microglial cells ($n = 9$ mice per group; two-sided Student's *t*-test). All data are presented as means ± s.e.m. *n* values represent the number of biologically independent experiments.

transcript was highly abundant in human microglia when compared with other cell types (Fig. 8a), suggesting a preponderant role of HIF1 in these cells. AD-associated microglial degeneration has mainly been observed in the human hippocampus[7,8]. To evaluate the potential contribution of HIF1 to AD, we measured the levels of *HIF1a* mRNA (by RT–qPCR) and HIF1α protein (by western blot) in hippocampal samples from individuals with AD and healthy control individuals (Supplementary Table 12). Both mRNA (a nonsignificant trend) and protein levels were upregulated, paralleling the progression of AD pathology (Fig. 8b). The drop in HIF1α levels at advanced (Braak V–VI) compared with intermediate (Braak III–IV) stages is probably explained by the dramatic end-stage cell death and atrophy. We also demonstrated upregulation of the mRNA levels of several HIF-regulated genes in AD (Braak V–VI) human hippocampal samples (Fig. 8c), suggesting that advanced stages of the pathology are associated with induction of HIF1.

Human microglial pathology is mainly concentrated in the hilar region of the dentate gyrus[8], a brain area with relatively low oxygen levels to preserve neurogenesis[45]. To investigate the contribution of hypoxia to microglial degeneration, we compared Aβ plaques from the dentate gyrus (hypoxia-prone region) with those from the perirhinal cortex (control region), as both brain areas accumulate similar large diffuse neuritic plaques[46]. Remarkably, a significant microglial depopulation of senile plaques was observed at Braak V–VI stages at the molecular layer of the dentate gyrus compared with plaques from the perirhinal cortex of the same individuals (Fig. 8d), suggesting that local hypoxia also primes AβAM dysfunction in the human AD brain, generating nude Aβ plaques.

An increase in plaque-associated axonal dystrophies has been observed in the brains of carriers of the AD-linked TREM2 variants[10,11], and sustained hypoxia incremented the local neuropathology in an AD mouse model (Fig. 7i,j). Therefore, we investigated whether nude Aβ plaques in the human dentate gyrus are also enriched in dystrophic neurites. Triple combined immunohistochemistry for p-TAU, IBA1 and Aβ in Braak V–VI hippocampal samples revealed plaques presenting dystrophic neurites in the zones that were devoid of microglia (Fig. 8e). To quantitatively demonstrate the relationship between nude Aβ plaques and increased local pathology, we measured the area occupied by IBA1 (microglia), AT8 (p-TAU) and Aβ per plaque. We anticipate that a microglial area lower than the Aβ area (protection index < 1, measured per individual plaque) should be less protected than Aβ plaques with larger microglial occupancy (protection index > 1) for the formation of AT8 reactive dystrophies. In fact, we demonstrated that Aβ plaques with a protection index of <1 presented higher dystrophic neurites (Fig. 8e). As a control, we also checked that both groups (protection index < 1 and protection index > 1) had similar Aβ plaque size distributions (Fig. 8e).

Altogether, our data strongly suggest that, similar to what was found in TREM2 risk allele carriers[10,11], nude Aβ plaques are associated with hypoxia-prone human brain areas and elevated local neuronal pathology in patients with AD.

Discussion

Increasing evidence indicates that the microglial defensive activity is required to halt the progression of AD[4,6,10–12]. At the same time,

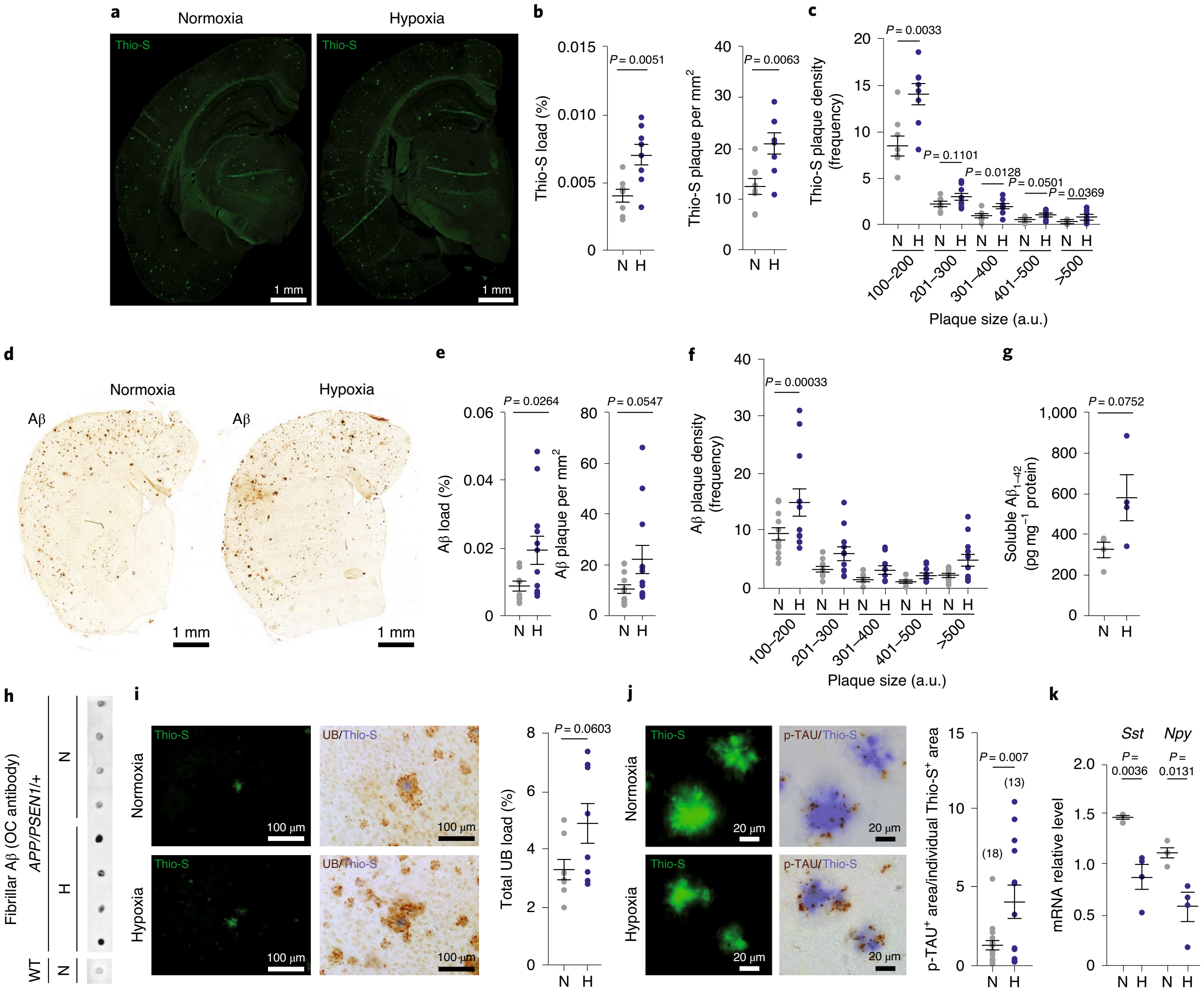

Fig. 7 | Systemic sustained hypoxia enhances Aβ aggregation, spreading and Aβ plaque-associated axonal dystrophy. a–k, 14-month-old *APP-PSEN1/+* mice were exposed to normoxia (N; 21% O_2) or sustained hypoxia (N; 9% O_2) for 21 d. **a**, Brain sections stained with Thio-S. **b**, Thio-S load (left) and plaque density (right) after exposure to normoxia and hypoxia ($n=8$; four mice per group; two-sided Student's *t*-test). **c**, Size distribution of Thio-S plaques after exposure to normoxia and hypoxia ($n=8$; four mice per group; two-sided Student's *t*-test). **d**, Brain sections stained for Aβ. **e**, Aβ load (left) and plaque density (right), estimated from brain slices after exposure to normoxia and hypoxia ($n=12$; four mice per group; two-sided Student's *t*-test). **f**, Size distribution of Aβ plaques after exposure to normoxia and hypoxia ($n=12$; four mice per group; two-sided Student's *t*-test). **g**, $Aβ_{1-42}$ levels quantified by ELISA in soluble brain extracts after exposure to normoxia and hypoxia ($n=4$ mice per group; two-sided Student's *t*-test). **h**, Fibrillar Aβ detected by dot blot in soluble cortical extracts exposed to normoxia and hypoxia ($n=4$ mice per group; a reference wild-type sample is shown). **i**, Left: cortical sections stained for ubiquitin (UB; right) and counterstained with Thio-S (left) under normoxia and hypoxia. Far right: quantification of the percentage of total ubiquitin load per slice after exposure to normoxia and hypoxia ($n=8$; four mice per group; two-sided Student's *t*-test). **j**, Left: cortical sections stained with Thio-S (left) and for p-TAU (right) after exposure to normoxia and hypoxia. Far right: quantification of the percentage of the individual Aβ plaque area occupied by p-TAU^+ neurites after exposure to normoxia and hypoxia (*n* values are provided in parentheses; two-sided Student's *t*-test). **k**, *Sst* and *Npy* mRNA levels estimated by RT–qPCR in hippocampal extracts from normoxic (gray bars) and hypoxic *APP-PSEN1/+* mice (blue bars). *Gapdh* mRNA was used as a housekeeping control ($n=4$; two-sided Student's *t*-test). All data are presented as means ± s.e.m. *n* values represent the number of biologically independent experiments.

microglia are the cells able to survive closer to Aβ deposits[18]. Therefore, to understand how these cells survive and provide a full response under challenging conditions is of utmost importance. We show here that AβAM are characterized by the paradoxical concomitant activation of HIF1-induced anaerobic glycolysis and aerobic respiration, suggesting local metabolic stress around Aβ plaques. We also show that sustained overactivation of HIF1 induces microglial quiescence in cellulo and a decrease in the ability of AβAM to proliferate and cluster around Aβ plaques in vivo. HIF1-mediated reduced coverage of Aβ plaques is associated with worsening of AD neuropathology both in AD mouse models and in the human AD brain, highlighting the relevance of modifiable AD risk factors related to HIF1 activation.

From their discovery, microglial cells were characterized by a surprising morphological plasticity[1,2], which is also observed around Aβ plaques, where microglia proliferate, migrate and emit thick

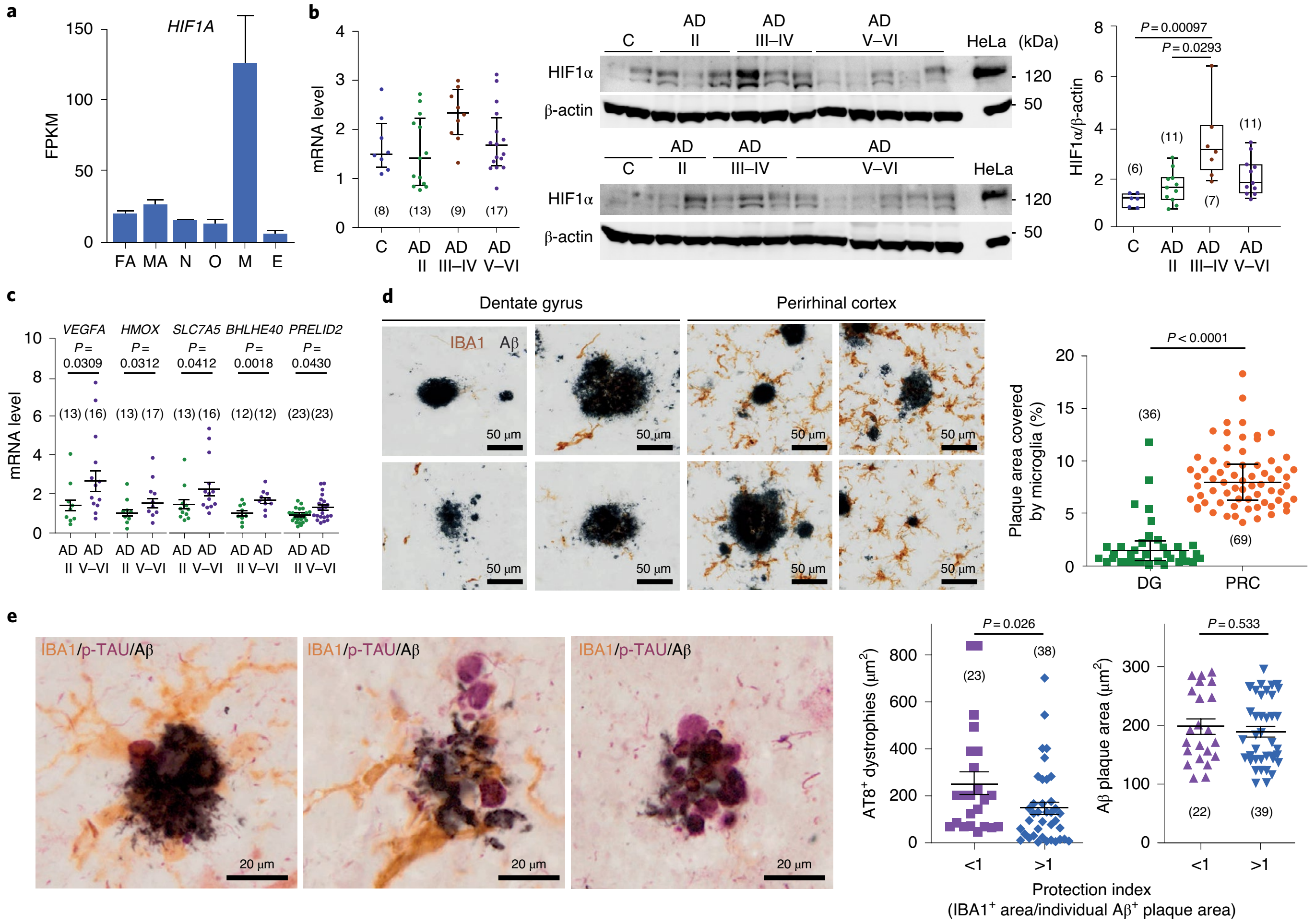

Fig. 8 | A human hypoxia-prone brain area contains nude Aβ plaques with increased local axonal dystrophy. **a**, Fragments per kilobase of *HIF1A* per million mapped reads (FPKM) in human brain cells (http://www.brainrnaseq.org/; ref. [44]). E, endothelial cells; FA, fetal astrocytes; M, microglia/macrophages; MA, adult astrocytes; N, neurons; O, oligodendrocytes. **b**, Left: *HIF1A* RT–qPCR of human hippocampus from control individuals (C; Braak I) and those with Braak stages II (ADII), III–IV (ADIII–IV) and V–VI (ADV–VI). The dots represent individual values (*n* values are provided in parentheses; Kruskal–Wallis test; $F = 7.124$; *GAPDH* used as a control). Middle: HIF1α in protein extracts from human hippocampus (β-actin control). Protein extract from HeLa cells under hypoxia (1% O_2; 4 h) were used as a HIF1α control. Right: box and whisker plot showing HIF1α/β-actin levels (*n* values are provided in parentheses; $F = 15.78$; Kruskal–Wallis test). **c**, mRNA levels estimated by RT–qPCR of human hippocampal samples (see **b**) (*n* values are provided in parentheses; Mann–Whitney *U*-test; $F = 32$ for *VEGFA*; $F = 28$ for *HMOX*; $F = 45$ for *SLC7A5*; $F = 20$ for *BHLHE40*; $F = 173$ for *PRELID2*). **d**, Left: staining of microglial cells (IBA1; brown) and Aβ plaques (dark blue) in the dentate gyrus (hypoxia-susceptible area) and perirhinal cortex (control brain area) of human AD brain (individuals with Braak V–VI). Right: plaque periphery covered by IBA1⁺ microglia (*n* values are provided in parentheses; three different individuals with AD; Mann–Whitney *U*-test). **e**, Left: staining of microglial cells (IBA1; brown), p-TAU⁺ dystrophic neurites (AT8; magenta) and Aβ plaques (dark blue) in the dentate gyrus of human AD brain (Braak V–VI). Right: axonal dystrophies (AT8⁺) and Aβ plaque area in samples with a protection index (IBA1⁺ area/individual Aβ⁺ plaques area ratio) of <1 or >1 (*n* values are provided in parentheses; Mann–Whitney *U*-test). All data are presented as means ± s.e.m., except in **b** (right), where the boxes represent the 25–75% percentiles, the central bars represent median values and the error bars represent the maximum and the minimum values. *n* values represent the number of biologically independent experiments.

cytoplasmic projections that constitute a physical barrier against Aβ spreading[4,10,11]. These morphologic adaptations are accompanied by exuberant transcriptional modulation that optimizes AβAM responses[14,26,27]. Between these transcriptional responses, we found that aerobic respiration is highly enriched in DAM transcription. In innate immune cells, HIF1 activation is normally associated with a metabolic switch from aerobic respiration to anaerobic glycolysis and activation of a proinflammatory program that includes cytokine production through increased inflammasome signaling[19,47]. It has been suggested that, in AD microglia, TREM2 activation could reduce this acute response to sustain long-term activity[17]. In light of our results, TREM2 activation entails aerobic respiration-based metabolism, which may counteract a switch towards a proinflammatory state of DAM. In AβAM, however, this equilibrium is at risk, as basal activity of HIF1 is detected and mitochondria elongate, a characteristic response of cells that maintain aerobic respiration under low oxygen and nutrient stress[35]. Mitochondrial elongation maximizes the functioning of the tricarboxylic acid cycle for biosynthesis and ATP production, sustaining cell viability under oxygen and nutrient deprivation, and prevents hypoxia- and/or low nutrient-induced mitophagy[36]. TREM2 activation of mTOR has been shown to be pivotal for microglial metabolic adaptation to confront Aβ deposition[17,20], and mitochondrial metabolism may be regulated by mTOR through increased translation of the mitochondrial transcription factor A (TFAM) and other key factors[33]. However, mTOR-mediated anabolic induction is reduced when the nutrient supply (including oxygen) is inadequate, via increased HIF1 transcription and translation. Further work will be required to demonstrate the role of the TREM2/mTOR pathway in regulation of mitochondrial AβAM metabolism.

The severe AβAM dependence on mitochondrial OXPHOS was revealed by forcing the inhibition of microglial mitochondrial activity via: (1) sustained hypoxia in cellulo, which induces a slowdown in microglial proliferation and quiescence; (2) in vivo VHL deficiency; or (3) in vivo sustained hypoxia, mimicking AD modifiable risk factors that reduce brain perfusion/oxygenation (for example, hypertension, obesity, atrial fibrillation, diabetes mellitus, physical inactivity, smoking[21] and intracerebral atherosclerosis[48]). Similarly, overactivation of HIF1 in microglia by systemic lipopolysaccharide injection also resulted in a shift towards anaerobic glycolysis, the production of proinflammatory cytokines and worsening of AD neuropathology[20]. Inversely, both sodium rutin (a natural flavonoid that induces a switch from anaerobic glycolysis to aerobic respiration in microglia) and interferon gamma (an inductor of mTOR) attenuated neuroinflammation[49], enhanced AβAM clustering and phagocytosis[24,49] and ameliorated the learning and memory defects observed in amyloidogenic models[24,49]. Interestingly, age (the main risk factor for AD[21]) may induce a decrease in the mouse microglial OXPHOS gene set (Extended Data Fig. 3c), suggesting that age could also merge with AD genetic[15–17,27] and modifiable risk factors in hijacking microglial aerobic respiration. The relationship between aging and microglial mitochondrial function will require additional experimental work.

The reduced AβAM proliferation and clustering by HIF1 overactivation resembles the phenotype observed in: (1) the brain of *TREM2* p.Arg47His and p.Arg62His carriers; (2) AD mouse models with genetic *Trem2* deficiency; and (3) AD mouse models expressing these AD-linked loss-of-function alterations[10,11]. It also resulted in increased neuropathology. Thus, in addition to other factors[23], systemic sustained hypoxia contributes to AD progression by decreasing the microglial ability to proliferate and confine Aβ deposits. Therefore, genetic (TREM2/apolipoprotein E), systemic (infections or brain hypoperfusion/hypoxia) and local stress (HIF1) factors converge in reducing AD microglial clustering and, therefore, their barrier function[6]. Correspondingly, a recent study highlighted the role of brain atherosclerosis in AD, suggesting a direct molecular link[48,50].

Of note, we also demonstrated that the human AD brain accumulates HIF1 and HIF1 targets, that a hypoxia-prone region is characterized by the presence of nude (microglia-free) Aβ plaques and that the absence of microglia correlates with increased periplaque p-TAU dystrophic neurites. Notably, recent epidemiologic studies have estimated that between one-third and one-half of AD cases could be attributable to modifiable risk factors[51–53] and have suggested that, as the age-adjusted incidence and prevalence of dementia might be decreasing (as reviewed in ref. [22]), AD may be preventable. Our results also pave the way for the search for pharmacologic agents that could improve the mitochondrial metabolic fitness of microglia against the stress imposed by Aβ plaques and, probably, reduce the progression of AD.

Methods

Human samples. Autopsy samples were obtained from the Neurological Tissue Bank of IDIBELL–Hospital of Bellvitge (Barcelona, Spain). The study (CEEA-US2017-13) was approved by the local ethics committee and the Comité de Ética de la Investigación (CEI), Hospital Virgen del Rocío, Seville, Spain. Samples with signed informed consent were obtained from Banco de Tejidos de la Fundación CIEN (Centro de Investigación de Enfermedades Neurológicas, Madrid, Spain) and the Neurological Tissue Bank of IDIBELL–Hospital of Bellvitge (Barcelona, Spain) and were classified by Braak tau pathology (Supplementary Table 12).

Mice. Mice were housed under controlled temperature (22 °C) and humidity conditions in a 12 h light/12 h dark cycle with ad libitum access to food and water. Housing and treatments were performed according to the animal care guidelines of the European Community Council (86/60/EEC). All animal procedures were conformed to under the Spanish law and approved (26/04/2016/064; Consejería de Agricultura, Pesca y Desarrollo Rural. Dirección General de la Producción Agrícola y Ganadera). Heterozygous B6.Cg-Tg(APPswe,PSEN1d9E)85Dbo/J (*APP-PSEN1*/+; stock number 34832-JAX), B6;C3-Tg(Prnp-MAPT*P301S) PS19Vle/J (TAU; stock number 008169), B6.129-*Hif1a*^{tm3Rsjo}/J (*Hif1a*$^{fl/fl}$; stock number 007561) and B6.129S4(C)-*Vhl*^{tm1Jae}/J (*Vhl*$^{fl/fl}$; stock number 012933) mice were obtained from The Jackson Laboratories. B6.129(C)-*Cx3cr1*$^{tm2.1(cre/ERT2)Jung}$/Orl (*Cx3cr1-Cre::ERT2* mice) were obtained from the European Mouse Mutant Archive (EMMA). APP mice (Sanofi) were provided by Transgenic Alliance–IFFA Credo. Wild-type mice were C57/Bl6J. To activate Cre::ERT2-mediated recombination, mice were fed for 30 d with a tamoxifen diet (400 mg tamoxifen citrate per kg; Envigo). All of the experiments were performed with a balanced number of male and female mice.

In vivo hypoxia treatment. Mice (14 months old) were chronically exposed to 9% O_2 using a specially designed hermetic chamber with O_2 and CO_2 controllers and temperature and humidity monitoring (Coy Laboratory Products). Light, feeding and cleaning cycles were kept uniform for all groups. Normoxic mice (controls) were also exposed to the same chamber but under 21% O_2.

BV2 cell line culture. The microglial cell line was obtained from the Interlab Cell Line Collection (National Institute of Cancer Research and Advanced Biotechnology Center, Italy). Cells were grown in RPMI 1640 medium (PAA) with 10% fetal bovine serum (Gibco), 2 mM L-glutamine (Gibco) and 1% penicillin/streptomycin (Gibco) in a water-saturated atmosphere of 5% CO_2 and 5% air. Cells were detached by trypsinization with 0.25% trypsin-EDTA (Gibco). Cells were always plated at 30–50% confluence to prevent anaerobic conditions and the activation of microglial cells.

Primary microglial cell cultures. Primary microglial cultures were prepared as previously described[8] from 1- to 3-d-old wild-type or *Cx3cr1-Cre::ERT2; Hif1a*$^{fl/fl}$ mouse brains.

In cellulo treatments. *Tamoxifen.* Primary microglial cultures were treated with 100 nM tamoxifen for 6 d before microglia isolation by mild trypsinization.

DMOG. Cells were incubated for 24 h in 1 or 0.1 mM DMOG dissolved in dimethyl sulfoxide. A similar amount of dimethyl sulfoxide was added to control cultures.

Hypoxia. Hypoxic conditions (1% O_2 and 5% CO_2) were achieved in a humidified variable aerobic workstation (InvivO2 300; Ruskinn).

Small interfering RNAs. BV2 cells were transfected with small interfering RNAs (20 nM) in suspension at 60–70% confluence for 48 h, using Lipofectamine 2000 (Invitrogen) as a transfection reagent following the manufacturer's instructions.

Flow cytometry. *Cell cycle analysis.* BV2 cells (1×10^6) were harvested, washed with phosphate-buffered saline (PBS), resuspended in 5 ml ice-cold 70% ethanol and left overnight at 4 °C. Cells were resuspended in 700 µl FACS/EDTA (5 mM), incubated at room temperature for 15 min, washed twice with 500 µl FACS/EDTA, resuspended in 800 µl FACS/EDTA supplemented with 0.2 mg ml^{-1} RNAse A (Qiagen) and incubated at 37 °C in agitation for 1.5 h. Before analysis, 0.04 mg ml^{-1} propidium iodide (Calbiochem) was added and the samples were incubated at 4 °C for 15 min in the dark. Cells were resuspended in 500 µl FACS/EDTA. Flow cytometry was performed in a BD LSRFortessa and cell cycle distribution was analyzed using BD FACSDiva software.

Acute isolation of microglia from adult brains. Isolated cells were stained with the antibodies CD11b-APC and CD45-PE at 4 °C for 30 min. Staining with isotype control-PE and isotype control-APC was used as a negative control. Both control and experimental samples were incubated with anti-CD16/CD32 blocker simultaneously. Cells were washed and sorted using a FACSAria Fusion (Becton Dickinson) flow cytometer and data were acquired and analyzed with FACSDiva software 8.0 (Becton Dickinson). The gating strategy and data analysis were performed according to guidelines[54]. To separate CLEC7a high and low populations, we used an anti-CD45-PE and an anti-CD11b-CFblue, with an anti-CLEC7a-FITC at room temperature for 20 min. An anti-CLEC7a-FMO control was included (cells stained with anti-CD45-PE and anti-CD11b-CFblue, but not with anti-CLEC7a-FITC) for autofluorescence values in the FITC channel.

RNA extraction and RT–qPCR. *Primary cultures, FACS-isolated microglia and mouse brain samples.* RNA was extracted using TRIzol reagent (Life Technologies). RNA samples (0.8 µg for mouse cortical samples and 0.5 µg for primary cultured microglia) were treated with PerfeCTa DNase (Quanta Biosciences) and copied to complementary DNA (cDNA) using qScript cDNA SuperMix (Quanta Biosciences). cDNA from FACS-isolated RNA microglia was amplified following the protocol described in the section 'Microarrays'. Real-time RT–qPCR was performed for all samples in a ViiA 7 Real-Time PCR System (Applied Biosystems) using either Power SYBR Green PCR Master Mix (Applied Biosystems) or iTaq Universal Probes Supermix (Bio-Rad) (Supplementary Table 13).

Human samples. Total RNA and proteins were extracted using TriPure Isolation Reagent (Roche). The RNA integrity (RIN) was determined by RNA 6000 Nano (Agilent). No significant differences between Braak groups were observed (RIN = 4.95 ± 1.4). Retrotranscription using 4 µg total RNA was performed with the High-Capacity cDNA Archive Kit (Applied Biosystems). 40 ng cDNA was mixed with 2× TaqMan Universal Master Mix (Applied Biosystems) and 20× TaqMan Gene Expression assay probes (Applied Biosystems) in an ABI Prism 7900HT (Applied Biosystems).

Microarrays. RNA quality was assessed using an Agilent 2100 Bioanalyzer (threshold RIN > 7). RNA amplification, cDNA hybridization and array scanning were performed using a GeneChip WT Pico Reagent Kit, Mouse Transcriptome 1.0 Array and Scanner 3000 Affymetrix. Raw data from Expression Console Software (Affymetrix) were exported to the R environment using LIMMA/Bioconductor packages (RStudio). Quality assessment, data normalization and differential expression analysis were performed using the arrayQualityMetrics package, robust multi-array method and LIMMA/Bioconductor package, respectively. The data are available from the Gene Expression Omnibus repository. Gene expression data from *5xfAD*, APP, TAU, Amyotrophic lateral sclerosis and aged mouse models were analyzed by GSEA using Biological Processes C5-v5.2, KEGG and the custom HMM, mTOR and MGnD gene sets.

Protein extraction and western blot. *Primary cultures.* Total proteins were extracted using TRIzol reagent (Life Technologies) according to the manufacturer's instructions. When blotting for HIF1α, samples were resuspended in lysis buffer 1 (30 mM Tris-HCl, 2 M thiourea, 7 M urea and 4% (wt/vol) CHAPS (pH 8.5)). An RC DC protein assay kit (Bio-Rad) was used for quantifications.

Human samples. Proteins were obtained from frozen human hippocampal tissue after sequential RNA and DNA extraction using TriPure Isolation Reagent (Roche). Protein pellets were solubilized using 4% (wt/vol) sodium dodecyl sulfate, 8 M urea and 40 mM Tris-HCl (pH 7.4) under rotation overnight at room temperature and quantified by Lowry assay. Western blots were performed using standard procedures. The antibodies used were anti-HIF1α (1:100), anti-NDUFS2 (1:1,000), anti-SDHA (1:1,000), anti-ATPsynβ (1:1,000), anti-RPL26 (1:1,000) and anti-β-actin (1:5,000). HRP-conjugated anti-rabbit (1:10,000) or anti-mouse (1:10,000) antibodies and a Western ECL Substrate kit (Bio-Rad) were used for signal detection.

Immunodetection. *In cellulo.* Microglial cultures plated on coverslips were stained under standard protocols with anti-IBA1 and anti-GFAP to detect astrocyte contamination. Images were taken with a BX61 microscope (Olympus).

BrdU staining. Cultures were incubated (3 h) in a media containing 10 µM BrdU (Sigma–Aldrich). Cells were fixed with ice-cold 4% paraformaldehyde for 10 min and permeabilized with ice-cold 70% ethanol at 4 °C overnight. Samples were treated with 2 M HCl for 15 min to denature the DNA, followed by incubation with 0.1 M sodium borate (pH 6.8) for 15 min.

Mice. The brains were removed from perfused mice with PBS and immediately fixed overnight (15 h) at 4 °C with 4% paraformaldehyde in PBS. Brains were paraffin embedded using an automatic tissue processor (ASP300S; Leica) and paraffin blocks cut into 20-µm-thick coronal sections using a microtome (RM2255; Leica). Immunostaining was performed according to standard protocols. The primary antibodies used were as follows: anti-IBA1 (1:500), anti-GFAP (1:1,000), anti-GS (1:1,000), anti-ubiquitin (1:400), anti-Aβ 6e10 (1:1,000), anti-NDUFS2 (1:1,000), anti-Ki67 (1:200) and anti-p-TAU (1:500). For immunohistochemistry, an EnVision+ kit (DAKO) was used for chromatic staining. Secondary antibodies were added and the reaction was developed with 3,3-diaminobenzidine (DAB; DAKO). For the immunofluorescence studies, we used secondary antibodies (anti-mouse or anti-rabbit) conjugated with Alexa Fluor 488 or Alexa Fluor 568. Tomato lectin staining was performed, incubating sections at 37 °C for 1 h, followed by Cy3-conjugated streptavidin (1:500). Thio-S, 4′,6-diamidino-2-phenylindole (DAPI) and Prussian blue stainings were used as counterstains.

Humans. For double-labeling light microscopy, sections were incubated with the microglial marker (anti-IBA1; 1:1,000), followed by the biotinylated secondary antibody and streptavidin-conjugated horseradish peroxidase. The peroxidase reaction was visualized with 0.05% 3-3-diaminobenzidine tetrahydrochloride (DAB; Sigma–Aldrich), 0.03% nickel ammonium sulfate and 0.01% hydrogen peroxide in PBS. After the DAB–nickel reaction (dark blue end product), sections were incubated with the anti-Aβ antibody (1:2,000). The second immunoperoxidase reaction was developed with DAB only (brown reaction end product). For triple immunolabeling, dark blue (anti-Aβ) and brown (anti-IBA1) peroxidase reactions were sequentially developed. Sections were then incubated with the p-TAU antibody (1:500) and visualized using the Vector VIP Peroxidase Substrate Kit (Vector Laboratories). Sections were then mounted on gelatin-coated slides, air dried, dehydrated in graded ethanol, cleared in xylene and coverslipped with DPX (BDH) mounting medium.

ISH and immunostaining. Brain tissues were cryoprotected in sucrose, embedded in OCT compound (Tissue-Tek) and kept at −80 °C. 10 µm coronal slices were obtained with a cryostat (Leica). The RNAScope 2.5 (ACD) protocol was used to detect *Hif1a* mRNA (ACD) according to the manufacturer's instructions, using a HybEZ oven (ACD). Subsequent immunostaining was performed for microglia staining (with the IBA1 marker) and nuclear staining (DAPI dye). After the RNAscope 2.5 protocol, slices were incubated for 10 min in PBS/Triton X-100 0.3% (vol/vol) and washed in PBS. Samples were incubated with anti-IBA1 antibody (1:500) O/N at 4 °C. Slices were then incubated with Alexa Fluor 488 anti-rabbit (1:400) for 1 h at room temperature and DAPI (Sigma–Aldrich; 1:1,000) stained before mounting with Fluoromount-G. Images were acquired using a confocal microscope (Nikon A1R+).

Electron microscopy. Mouse brains were processed according to standard protocols for electron microscopy visualization. Selected areas were cut into ultrathin sections, stained with uranyl acetate and lead citrate and examined with an electron microscope (JEM-1400; JEOL). Quantification of mitochondrial morphology was performed in Fiji by measuring the area, perimeter and major and minor axes. The Fit Ellipse function was used to calculate the major and minor axes. The circularity ($4\pi \times \text{area}/\text{perimeter}^2$) and aspect ratio (major axis/minor axes) were calculated. For circularity, a value of 1.0 indicates a perfect circle. As the value approaches 0, it indicates an increasingly elongated shape.

Bioenergetic analysis of primary microglial cell cultures. *Seahorse Extracellular Flux (XFp) Analyzer (Agilent).* Primary microglial cells (3.5×10^4 cells per well) were seeded (80 µl per well) in XFp cell culture mini plates and incubated at 37 °C in a humidified incubator with 5% CO_2 for 24 h in their cell growth medium. For the mitochondrial stress test, oligomycin (20 µM), carbonyl cyanide-*p*-trifluoromethoxyphenylhydrazone (20 µM) and rotenone/antimycin A (10 µM) (all Agilent Seahorse) were loaded for sequential delivery. For the glycolytic rate assay test, rotenone/antimycin A (10 µM) and 2-deoxy-D-glucose (500 mM) (both Agilent Seahorse) were similarly loaded. Following calibration, the oxygen consumption rate (OCR), extracellular acidification rate (ECAR) and PER were measured every 6 min for 72 min and the compounds were injected sequentially at 18-min intervals. The OCR, ECAR and PER were automatically calculated using Seahorse XFp software, and four to six biologically independent replicates were assessed for each condition.

Microglial coverage and stereological quantification. *Human periplaque coverage.* The periplaque microglial coverage was defined as the percentage of area stained with IBA1 in the periplaque area (delimited by drawing a circle 30 µm from the plaque edge). Images of IBA1/4G8-stained sections were acquired using the automated digital microscopy system (Olympus VS120) connected to an Olympus BX61VS with a high-resolution digital color camera (VC50 Olympus). Images from plaques of the different brain areas (the dentate gyrus and perirhinal cortex) were then acquired using OlyVIA 2.6 image viewer software (Olympus) (image size = 1,654 pixels × 877 pixels; pixel size = 28.34 pixels per cm). Digital images ($n = 3$ individuals; Braak V–VI) were processed using the Visilog 6.3 (Noesis) image analysis system.

Dystrophy pathology related to microglial coverage. Dystrophy pathology related to microglial coverage was quantified per plaque, analyzing the percentages of areas stained with AT8 (p-TAU) or IBA1 in the plaque area. Images of AT8/IBA1/4G8 triple-immunostained sections from the dentate gyrus were acquired using the digital microscopy system (Olympus VS120), as described for periplaque coverage quantification. Digital images were processed using Fiji (ImageJ). Three different binary masks (AT8-, IBA1- and 4G8-reactive areas) were generated using the color threshold segmentation (HSB mode) and each selected area was measured. Finally, the protection index was calculated as the ratio of IBA1/Aβ plaque.

Number, coverage of mouse Aβ plaques and proliferative microglia. Amyloid plaques were visualized with Thio-S staining and were randomly selected blind to the treatment in the cortex and hippocampus. Quantifications were done in superimages generated with the NewCAST system (Visiopharm) associated with the BX61 microscope (Olympus). The number of microglial cells surrounding amyloid plaques was determined after immunostaining for IBA1 and staining with DAPI using immunofluorescence. The microglial coverage of individual amyloid plaques was obtained by normalizing the IBA1-occupied area by the area occupied for the corresponding Thio-S reactive plaque, calculated from binary masks generated with the appropriate thresholds for all images in Fiji. The results are presented as a percentage of IBA1 per Aβ plaque area. Proliferative microglia were identified as double reactive for Ki67 and IBA1. To quantify different signals around Aβ plaques, we drew a 50-µm-radius circle and quantified the density using Fiji (ISH *Hif1a* mRNA and NDUFS2). In the wild type and regions distal to Aβ plaques, full images were quantified and a density of the marker was calculated.

Microglial stereology. The measurements were performed blind to the treatment. This was an unbiased stereological approach using an Olympus BX61 microscope combined with the CAST system. The sample area was then manually outlined, the total area was quantified using CAST software and microglia between two specific bregma points were estimated using a dissector area of 28,521.3 μm^2 (CAST). The dentate gyrus was chosen as a sample area.

Amyloid plaque quantification. These measurements were blind to the treatment. Quantifications were done in superimages generated with the NewCAST system (Visiopharm) associated with the BX61 microscope (Olympus).

Load. The Thio-S and Aβ plaque loads were estimated using Fiji. A segmented binary mask was generated and the area occupied by detected particles over a specific constant threshold was quantified. The load was defined as the percentage of the total cortex area occupied by Thio-S and Aβ.

Density. This parameter was calculated by dividing the number of detected particles obtained in parallel to the load quantification described above by the sampled cortical area.

Frequency. The size of each detected particle obtained with the load quantification above was registered and the density was calculated for different intervals of plaque size.

Dystrophic neurite quantification. Amyloid plaques were visualized upon Thio-S staining. These measurements were blind to the treatment. Quantifications were done in superimages generated with the NewCAST system (Visiopharm) associated with the BX61 microscope (Olympus).

Ubiquitin load. The ubiquitin load was estimated using Fiji. A segmented binary mask was generated and the area occupied by detected particles over a specific constant threshold was quantified. The load was defined as the percentage of the cortical brain area occupied by ubiquitin.

p-TAU load. Plaques were randomly selected by Thio-S staining and the Thio-S and p-TAU areas were estimated using Fiji in individual plaques. The results are presented as a percentage of the p-TAU area per amyloid plaque area.

Aβ ELISA. For soluble $A\beta_{1-42}$ quantification, proteins were extracted from acutely dissected hemibrains using a Dounce's homogenizer in PBS (8× wet weight/volume buffer) containing phosphatase and protease inhibitors (Sigma–Aldrich; 1:1,000). Samples were consecutively centrifuged at 600, 15,000 and 100,000*g* in an Optima MAX ultracentrifuge (Beckman Coulter) at 4 °C. The supernatant was carefully decanted and stored on ice until it was used for the assay. For standard curve samples, lyophilized $A\beta_{1-42}$ synthetic peptide (AnaSpec) was used. A Human $A\beta_{1-42}$ ELISA Kit (Invitrogen) was used following the manufacturer's instructions. Measurements were normalized by protein levels using the RC DC protein assay kit (Bio-Rad).

Dot blot. Cortical soluble extracts were obtained as described for soluble Aβ quantification. Total protein was quantified with the RC DC kit (Bio-Rad) according to the manufacturer's guidelines and using bovine serum albumin for the standard curve. 1 μg of each soluble extract was spotted onto a nitrocellulose membrane (GE Healthcare) and air dried for 30 min. The membrane was incubated overnight with the primary antibody OC (Millipore; 1:5,000). Signal detection was performed using a secondary HRP-conjugated anti-rabbit antibody and Western ECL Substrate kit (Bio-Rad).

Statistical analysis. All individual measurements constitute biological replicates. Samples with $n < 9$ were analyzed using parametric tests. Samples with $n \geq 9$ were evaluated for normal distribution using D'Agostino and Pearson's omnibus normality test. Comparisons between two groups were performed with a two-sided unpaired Student's *t*-test, whereas comparisons between more than two groups were done with analysis of variance (ANOVA) with Tukey's test. The data are expressed as means ± s.e.m., as specified in the figure captions. $P \leq 0.05$ was considered statistically significant. For human samples, different groups were compared using the Mann–Whitney *U*-test. Statistical analyses and graphs were performed/generated in GraphPad Prism version 9.0 (GraphPad).

Reporting Summary. Further information on research design is available in the Nature Research Reporting Summary linked to this article.

Data availability

Transcriptomics data are available from the Gene Expression Omnubus with the following accession numbers: GSE97423 (mouse primary microglial cultures exposed to normoxia or hypoxia); GSE129296 (isolated Clec7a$^+$ microglia from wild-type, APP and TAU mice); and GSE168059 (isolated microglia from *APP-PSEN1/+*; *VHL*$^{fl/-}$ with or without tamoxifen treatment). Source data are provided with this paper.

Received: 17 July 2020; Accepted: 8 March 2021;

References

1. Del Río-Hortega, P. El 'tercer elemento' de los centros nerviosos. I. La microglía en estado normal. *Bol. Soc. Esp. Biol.* **VIII**, 69–82 (1919).
2. Del Río-Hortega, P. El 'tercer elemento' de los centros nerviosos. II. Intervención de la microglía en los procesos patológicos (células en bastoncito y cuerpos gránulo-adiposos). *Bol. Soc. Esp. Biol.* **VIII**, 91–103 (1919).
3. Sierra, A. et al. The "Big-Bang" for modern glial biology: translation and comments on Pío del Río-Hortega 1919 series of papers on microglia. *Glia* **64**, 1801–1840 (2016).
4. Condello, C., Yuan, P., Schain, A. & Grutzendler, J. Microglia constitute a barrier that prevents neurotoxic protofibrillar Aβ42 hotspots around plaques. *Nat. Commun.* **6**, 6176 (2015).
5. Bertram, L. & Tanzi, R. E. Alzheimer disease risk genes: 29 and counting. *Nat. Rev. Neurol.* **15**, 191–192 (2019).
6. Colonna, M. & Wang, Y. TREM2 variants: new keys to decipher Alzheimer disease pathogenesis. *Nat. Rev. Neurosci.* **17**, 201–207 (2016).
7. Streit, W. J., Xue, Q. S., Tischer, J. & Bechmann, I. Microglial pathology. *Acta Neuropathol. Commun.* **2**, 142 (2014).
8. Sanchez-Mejias, E. et al. Soluble phospho-tau from Alzheimer's disease hippocampus drives microglial degeneration. *Acta Neuropathol.* **132**, 897–916 (2016).
9. Lassmann, H. et al. Cell death in Alzheimer's disease evaluated by DNA fragmentation in situ. *Acta Neuropathol.* **89**, 35–41 (1995).
10. Yuan, P. et al. TREM2 haplodeficiency in mice and humans impairs the microglia barrier function leading to decreased amyloid compaction and severe axonal dystrophy. *Neuron* **90**, 724–739 (2016).
11. Leyns, C. E. G. et al. TREM2 function impedes tau seeding in neuritic plaques. *Nat. Neurosci.* **22**, 1217–1222 (2019).
12. Wang, Y. et al. TREM2-mediated early microglial response limits diffusion and toxicity of amyloid plaques. *J. Exp. Med.* **213**, 667–675 (2016).
13. Lucin, K. M. & Wyss-Coray, T. Immune activation in brain aging and neurodegeneration: too much or too little? *Neuron* **64**, 110–122 (2009).
14. Holtman, I. R. et al. Induction of a common microglia gene expression signature by aging and neurodegenerative conditions: a co-expression meta-analysis. *Acta Neuropathol. Commun.* **3**, 31 (2015).
15. Sala Frigerio, C. et al. The major risk factors for Alzheimer's disease: age, sex, and genes modulate the microglia response to Aβ plaques. *Cell Rep.* **27**, 1293–1306 (2019).
16. Ulrich, J. D. et al. ApoE facilitates the microglial response to amyloid plaque pathology. *J. Exp. Med.* **215**, 1047–1058 (2018).
17. Ulland, T. K. et al. TREM2 maintains microglial metabolic fitness in Alzheimer's disease. *Cell* **170**, 649–663 (2017).
18. Serrano-Pozo, A. et al. Differential relationships of reactive astrocytes and microglia to fibrillar amyloid deposits in Alzheimer disease. *J. Neuropathol. Exp. Neurol.* **72**, 462–471 (2013).
19. Kaelin, W. G. & Ratcliffe, P. J. Oxygen sensing by metazoans: the central role of the HIF hydroxylase pathway. *Mol. Cell* **30**, 393–402 (2008).
20. Wendeln, A.-C. et al. Innate immune memory in the brain shapes neurological disease hallmarks. *Nature* **556**, 332–338 (2018).
21. Livingston, G. et al. Dementia prevention, intervention, and care. *Lancet* **390**, 2673–2734 (2017).
22. Serrano-Pozo, A. & Growdon, J. H. Is Alzheimer's disease risk modifiable? *J. Alzheimers Dis.* **67**, 795–819 (2019).
23. Zlokovic, B. V. Neurovascular pathways to neurodegeneration in Alzheimer's disease and other disorders. *Nat. Rev. Neurosci.* **12**, 723–738 (2011).
24. Baik, S. H. et al. A breakdown in metabolic reprogramming causes microglia dysfunction in Alzheimer's disease. *Cell Metab.* **30**, 493–507.e6 (2019).
25. Puente-Santamaria, L., Wasserman, W. W. & Del Peso, L. TFEA.ChIP: a tool kit for transcription factor binding site enrichment analysis capitalizing on ChIP-seq datasets. *Bioinformatics* **35**, 5339–5340 (2019).
26. Keren-Shaul, H. et al. A unique microglia type associated with restricting development of Alzheimer's disease. *Cell* **169**, 1276–1290 (2017).
27. Krasemann, S. et al. The TREM2–APOE pathway drives the transcriptional phenotype of dysfunctional microglia in neurodegenerative diseases. *Immunity* **47**, 566–581 (2017).
28. Chiu, I. M. et al. A neurodegeneration-specific gene-expression signature of acutely isolated microglia from an amyotrophic lateral sclerosis mouse model. *Cell Rep.* **4**, 385–401 (2013).
29. Hickman, S. E. et al. The microglial sensome revealed by direct RNA sequencing. *Nat. Neurosci.* **16**, 1896–1905 (2013).
30. Wang, Y. et al. TREM2 lipid sensing sustains the microglial response in an Alzheimer's disease model. *Cell* **160**, 1061–1071 (2015).
31. Grubman, A. et al. A single-cell atlas of entorhinal cortex from individuals with Alzheimer's disease reveals cell-type-specific gene expression regulation. *Nat. Neurosci.* **22**, 2087–2097 (2019).

32. Morita, M. et al. mTORC1 controls mitochondrial activity and biogenesis through 4E-BP-dependent translational regulation. *Cell Metab.* **18**, 698–711 (2013).
33. Morita, M. et al. mTOR coordinates protein synthesis, mitochondrial activity and proliferation. *Cell Cycle* **14**, 473–480 (2015).
34. Steinman, J., Sun, H.-S. & Feng, Z.-P. Microvascular alterations in Alzheimer's disease. *Front. Cell. Neurosci.* **14**, 457–469 (2021).
35. Li, J. et al. Mitochondrial elongation-mediated glucose metabolism reprogramming is essential for tumour cell survival during energy stress. *Oncogene* **36**, 4901–4912 (2017).
36. Gomes, L. C. & Scorrano, L. Mitochondrial elongation during autophagy. *Autophagy* **7**, 1251–1253 (2011).
37. Ginouvès, A., Ilc, K., Macías, N., Pouysségur, J. & Berra, E. PHDs overactivation during chronic hypoxia "desensitizes" HIFα and protects cells from necrosis. *Proc. Natl Acad. Sci. USA* **105**, 4745–4750 (2008).
38. Berra, E. et al. HIF prolyl-hydroxylase 2 is the key oxygen sensor setting low steady-state levels of HIF-1α in normoxia. *EMBO J.* **22**, 4082–4090 (2003).
39. Bondolfi, L. et al. Amyloid-associated neuron loss and gliogenesis in the neocortex of amyloid precursor protein transgenic mice. *J. Neurosci.* **22**, 515–522 (2002).
40. Papandreou, I., Cairns, R. A., Fontana, L., Lim, A. L. & Denko, N. C. HIF-1 mediates adaptation to hypoxia by actively downregulating mitochondrial oxygen consumption. *Cell Metab.* **3**, 187–197 (2006).
41. Zhou, Y., Ulland, T. K. & Colonna, M. TREM2-dependent effects on microglia in Alzheimer's disease. *Front. Aging Neurosci.* **10**, 202 (2018).
42. Serrano-Pozo, A. et al. Acute and chronic sustained hypoxia do not substantially regulate amyloid-β peptide generation in vivo. *PLoS ONE* **12**, e0170345 (2017).
43. Ramos, B. et al. Early neuropathology of somatostatin/NPY GABAergic cells in the hippocampus of a PS1×APP transgenic model of Alzheimer's disease. *Neurobiol. Aging* **27**, 1658–1672 (2006).
44. Zhang, Y. et al. Purification and characterization of progenitor and mature human astrocytes reveals transcriptional and functional differences with mouse. *Neuron* **89**, 37–53 (2016).
45. Chatzi, C., Schnell, E. & Westbrook, G. L. Localized hypoxia within the subgranular zone determines the early survival of newborn hippocampal granule cells. *eLife* **4**, e08722 (2015).
46. Thal, D. R. et al. Sequence of Aβ-protein deposition in the human medial temporal lobe. *J. Neuropathol. Exp. Neurol.* **59**, 733–748 (2000).
47. Weichhart, T., Hengstschläger, M. & Linke, M. Regulation of innate immune cell function by mTOR. *Nat. Rev. Immunol.* **15**, 599–614 (2015).
48. Wingo, A. P. et al. Shared proteomic effects of cerebral atherosclerosis and Alzheimer's disease on the human brain. *Nat. Neurosci.* **23**, 696–700 (2020).
49. Pan, R.-Y. et al. Sodium rutin ameliorates Alzheimer's disease-like pathology by enhancing microglial amyloid-β clearance. *Sci. Adv.* **5**, eaau6328 (2019).
50. Iadecola, C. Revisiting atherosclerosis and dementia. *Nat. Neurosci.* **23**, 41–42 (2020).
51. Ashby-Mitchell, K., Burns, R., Shaw, J. & Anstey, K. J. Proportion of dementia in Australia explained by common modifiable risk factors. *Alzheimers Res. Ther.* **9**, 11 (2017).
52. Norton, S., Matthews, F. E., Barnes, D. E., Yaffe, K. & Brayne, C. Potential for primary prevention of Alzheimer's disease: an analysis of population-based data. *Lancet Neurol.* **13**, 788–794 (2014).
53. Barnes, D. E. & Yaffe, K. The projected effect of risk factor reduction on Alzheimer's disease prevalence. *Lancet Neurol.* **10**, 819–828 (2011).
54. Herzenberg, L. A., Tung, J., Moore, W. A., Herzenberg, L. A. & Parks, D. R. Interpreting flow cytometry data: a guide for the perplexed. *Nat. Immunol.* **7**, 681–685 (2006).

Acknowledgements

We thank P. J. Ratcliffe for hosting A.H.-G. in his laboratory for the conduction of PhD experiments and L. del Peso for assistance with transcription factor enrichment analysis. We also thank K. Levitsky (microscopy), M. J. Castro (flow cytometry), F. J. Moron (genomics), E. Andres-Leon (bioinformatics), and R. Duran (histology) for advice and technical assistance in relation to experiments performed at the IBiS core facilities. R.M.-D. was the recipient of a Sara Borrell fellowship from Instituto de Salud Carlos III (ISCIII) (CD09/0007). N.L.-U., C.O.-d.S.L., C.R.-M. and M.I.A.-V. were the recipients of FPU fellowships from Spanish Ministry of Education, Culture and Sport (FPU14/02115, AP2010-1598, FPU16/02050 and FPU15/02898, respectively). A.H.-G. was the recipient of an FPI fellowship from the Spanish Ministry of Education, Culture and Sport (BES-2010-033886). This work was supported by grants from the Spanish MINEICO, ISCIII and FEDER (European Union) (SAF2012-33816, SAF2015-64111-R, SAF2017-90794-REDT and PIE13/0004 to A.P.); by the Regional Government of Andalusia co-funded by CEC and FEDER funds (European Union) ('Proyectos de Excelencia'; P12-CTS-2138 and P12-CTS-2232 to A.P.); by the 'Ayuda de Biomedicina 2018', Fundación Domingo Martínez (to A.P.) ; by the ISCIII of Spain, co-financed by FEDER funds (European Union) through grants PI18/01556 (to J.V.) and PI18/01557 (to A. Gutierrez); by Junta de Andalucía, co-financed by FEDER funds (grants UMA18-FEDERJA-211 (to A. Gutierrez) and US-1262734 (to J.V.)); and by Spanish MINEICO (BFU2016-76872-R and BES-2011-047721 to E.B.).

Author contributions

A.P., J.V., R.M.-D., N.L.-U., C.R.-M., A.H.-G. and C.O.-d.S.L. conceived of and designed the research. A.P., R.M.-D., N.L.-U., C.R.-M., A.H.-G., C.O.-d.S.L., M.I.A.-V., M.A.S.-G., E.S.-M., J.C.D., A.E.R.-N., V.N., A.G.-A., M.V.S.-M., A.V. and A. Gerpe performed the research. R.M.-D., N.L.-U., C.R.-M., A.H.-G., C.O.-d.S.L., M.I.A.-V., M.A.S.-G., E.S.-M., J.C.D., A.E.R.-N., C.F., V.N., A.G.-A., M.V.S.-M., A.V., A. Gutierrez, M.V., T.B., A.S.-P., J.L.-B., E.B., J.V. and A.P. analyzed the data. E.J.H. and T.B. provided methodological and/or scientific assistance. E.J.H. and T.B. contributed mouse models/samples. A.P., E.B., J.V. and A.S.-P. wrote the manuscript.

Competing interests

The authors declare no competing interests.

Additional information

Supplementary information The online version contains supplementary material available at https://doi.org/10.1038/s43587-021-00054-2.

Correspondence and requests for materials should be addressed to J.V. or A.P.

Peer review information: *Nature Aging* thanks Luca Scorrano and the other, anonymous, reviewer(s) for their contribution to the peer review of this work.

Reprints and permissions information is available at www.nature.com/reprints.

Publisher's note: Springer Nature remains neutral with regard to jurisdictional claims in published maps and institutional affiliations.

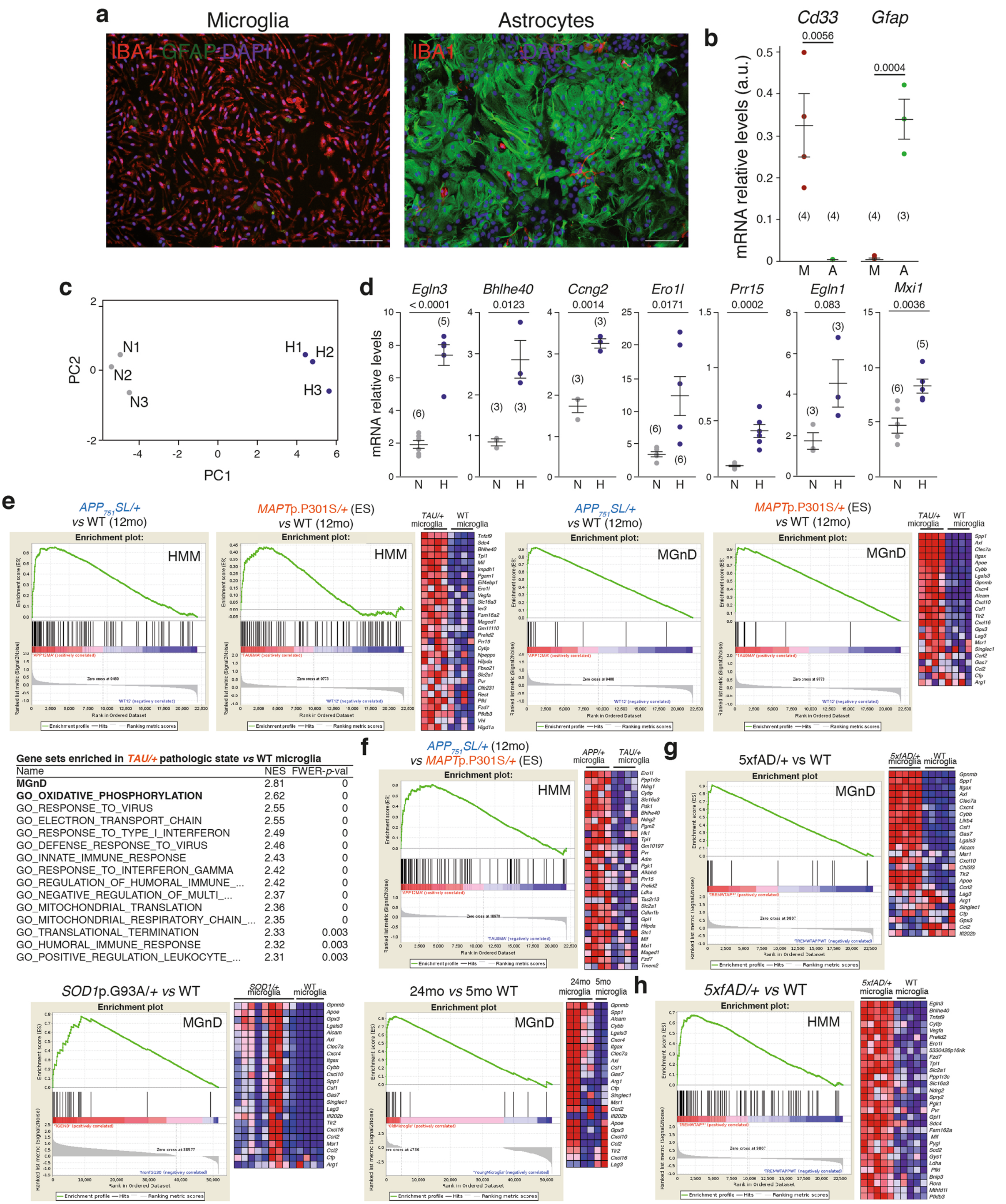

Gene sets enriched in *TAU/+* pathologic state *vs* WT microglia

Name	NES	FWER-*p*-val
MGnD	2.81	0
GO_OXIDATIVE_PHOSPHORYLATION	2.62	0
GO_RESPONSE_TO_VIRUS	2.55	0
GO_ELECTRON_TRANSPORT_CHAIN	2.55	0
GO_RESPONSE_TO_TYPE_I_INTERFERON	2.49	0
GO_DEFENSE_RESPONSE_TO_VIRUS	2.46	0
GO_INNATE_IMMUNE_RESPONSE	2.43	0
GO_RESPONSE_TO_INTERFERON_GAMMA	2.42	0
GO_REGULATION_OF_HUMORAL_IMMUNE_...	2.42	0
GO_NEGATIVE_REGULATION_OF_MULTI_...	2.37	0
GO_MITOCHONDRIAL_TRANSLATION	2.36	0
GO_MITOCHONDRIAL_RESPIRATORY_CHAIN_...	2.35	0
GO_TRANSLATIONAL_TERMINATION	2.33	0.003
GO_HUMORAL_IMMUNE_RESPONSE	2.32	0.003
GO_POSITIVE_REGULATION_LEUKOCYTE_...	2.31	0.003

Extended Data Fig. 1 | See next page for caption.

Extended Data Fig. 1 | HIF1-mediated transcription in DAM. **a**, Immunocytochemistry of primary cultures of microglia (left panel) and astrocytes (right panel) using antibodies against IBA1 (red) and GFAP (green). Scale bar is 20 µm. **b**, Relative levels of *Cd33* and *Gfap* mRNAs estimated by qRT-PCR (a.u. arbitrary units) in microglial (M) and astrocyte cultures (A). *Hmbs* levels were used as housekeeping control (*n* is indicated between brackets, independent cultures, Student's t-test, two-sided). **c**, Principal component analysis showing the separation between biological replicates of mouse primary microglial cell cultures exposed to normoxia (N: 21% O_2, 6 h) or hypoxia (H: 1% O_2, 6 h). **d**, Primary microglial cell cultures were exposed to N or H (24 h) and the relative levels of several mRNAs included in the HIF1/hypoxia-induced microglial module (HMM) were estimated by qRT-PCR. *Hmbs* levels were used as housekeeping control (*n* is indicated between brackets, biological independent cultures, Student's t-test, two-sided). **e–h**, Gene set enrichment analysis (GSEA). **e**, GSEA of *APP*$_{751}$*SL/+* (left and middle right) or *MAPT*p301S/+ end-stage (ES) (middle left and right) DAM *versus* (*vs*) wild-type (WT) 12-month-old (mo) microglia. Enrichment plots of the HMM (left) and MGnD (right) GSs. The table contains the 15 top GSs with a FWER-p-value less than 0.05. **f**, GSEA of *APP*$_{751}$*SL/+ versus* (*vs*) *MAPT*p301S/+ end-stage (ES). **g**, **h**, GSEA *5xfAD/+* DAM *vs* wild-type (WT) microglia (**g**, upper row MGnD GS; **h**, HMM GS); *SOD1*p.G93A/+ DAM *vs* WT microglia (**g**, left in the lower row); 24-mo *vs* 5-mo WT microglia (**g**, right in the lower row). Data are represented as mean ± S.E.M.

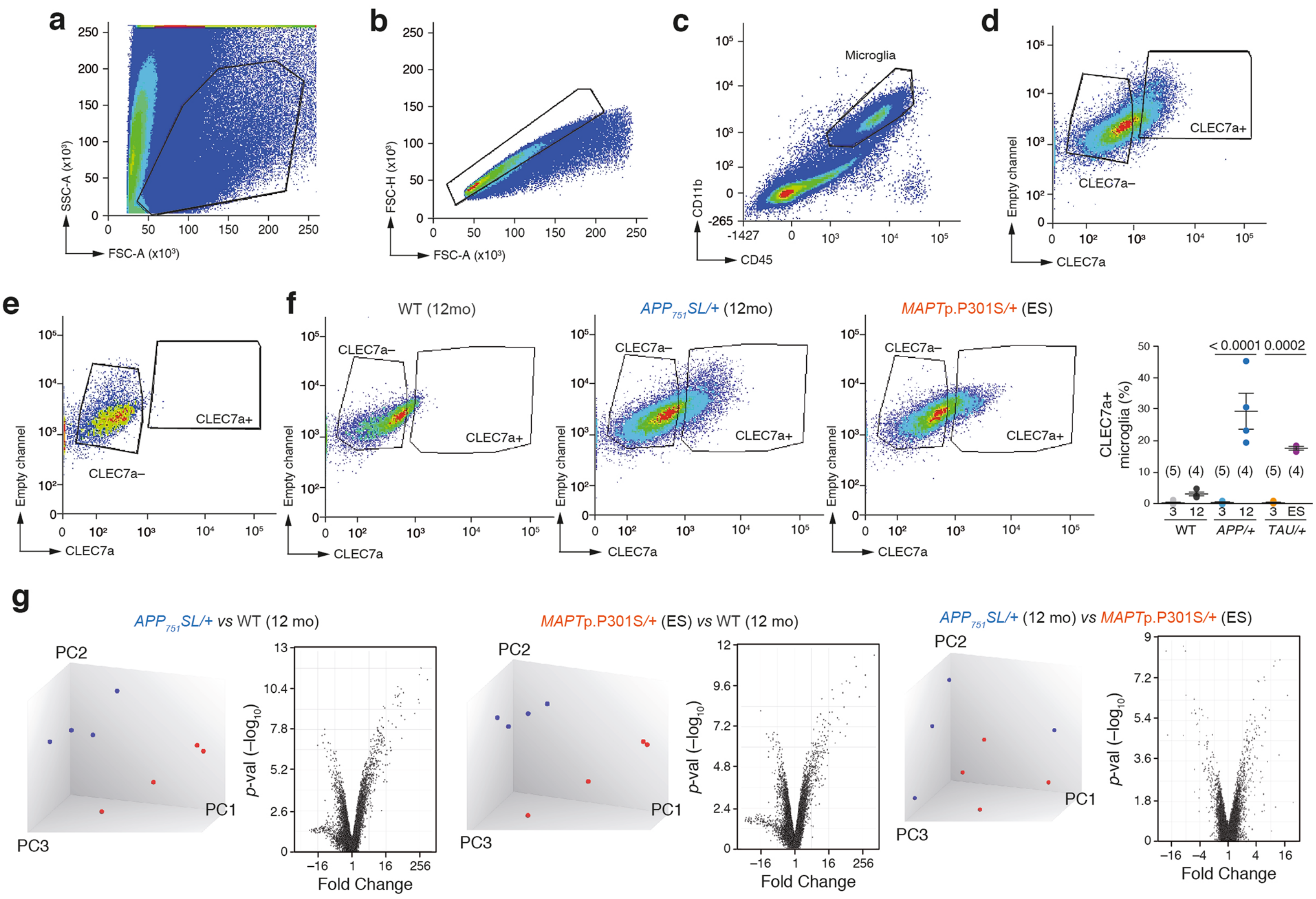

Extended Data Fig. 2 | Gating strategy to isolate CLEC7a⁺ microglia. Gate identification was performed according to guidelines and previous reports in contour density plots. **a**, Debris, and dead cells were discarded by forward (FSC) and side (SSC) scatters dispersion of events. **b**, Singlets of events were selected according to FSC height (FSC-H) versus area (FSC-A). **c**, Microglial cells, reactive for CD45 and CD11b markers, were selected (black box). **d, e**, The gate selected to isolate CLEC7a⁺ microglia is shown in (**d**) and was defined by performing the same experiment without CLEC7a antibody (**e**). **f**, Flow cytometry contour density plots of CD11b/CD45 reactive microglia with low (CLEC7a⁻) and high (CLEC7a⁺) levels. Right graph represents the percentage of Clec7a⁺ microglia in each experimental group; wild-type (WT), *APP*$_{751}$*SL/+* (*APP/+*) and *MAPT*p301S/+ (*TAU/+*); (*n* is indicated between brackets, biological independent experiments, ANOVA, Tukey's test). **g**, Principal component analysis (left panels) and volcano plots (right panels) of the microarray studies presented in Figs. 1 and 2. Data are represented as mean ± S.E.M.

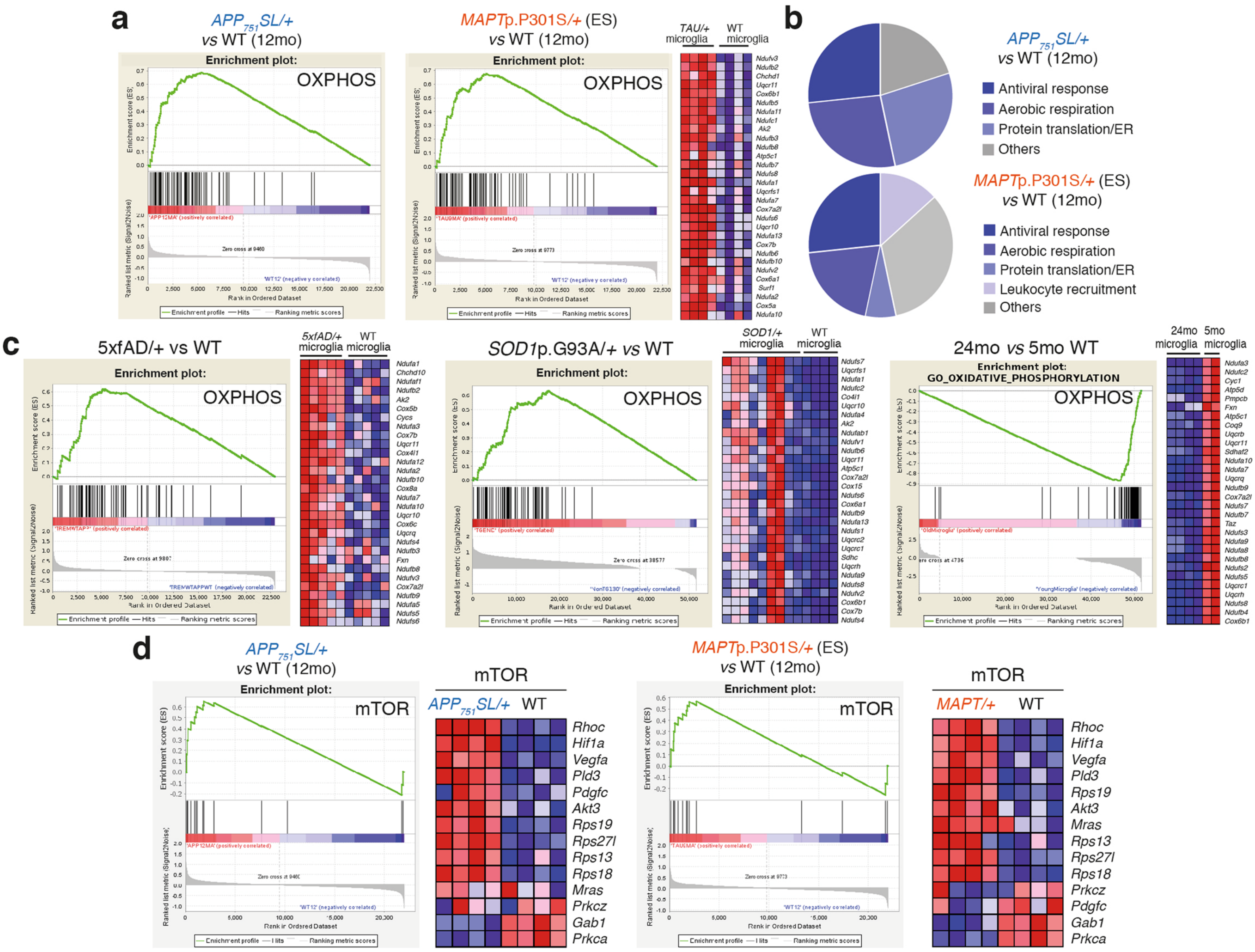

Extended Data Fig. 3 | Mitochondrial activation in DAM. a, GSEA of *APP*$_{751}$*SL*/+ (left) or *MAPT*p301S/+ ES DAM (middle and right) *versus* (*vs*) wild-type (WT) 12mo microglia. Enrichment plots and heat maps (middle) of top 30 ranking leading edge genes of the oxidative phosphorylation (OXPHOS) GS. Red symbolizes overexpression and blue down regulation (see Supplementary Data Table for shade values). **b**, Sector graphs of the most enriched biological functions between the 15 top GSs enriched in *APP*$_{751}$*SL*/+ and *MAPT*p.P301S/+ DAM *vs* WT microglia. **c**, GSEA of *5xfAD*/+; *SOD1*p.G93A/+, and aged (24mo) DAM *vs* WT age matched or young (5mo) microglia. Enrichment plots and heat maps of up to the top 30 ranking leading edge genes of OXPHOS GS. **d**, GSEA of *APP*$_{751}$*SL*/+ DAM *vs* wild-type (WT) 12mo microglia. Enrichment plot of the oxidative phosphorylation (OXPHOS) GS.

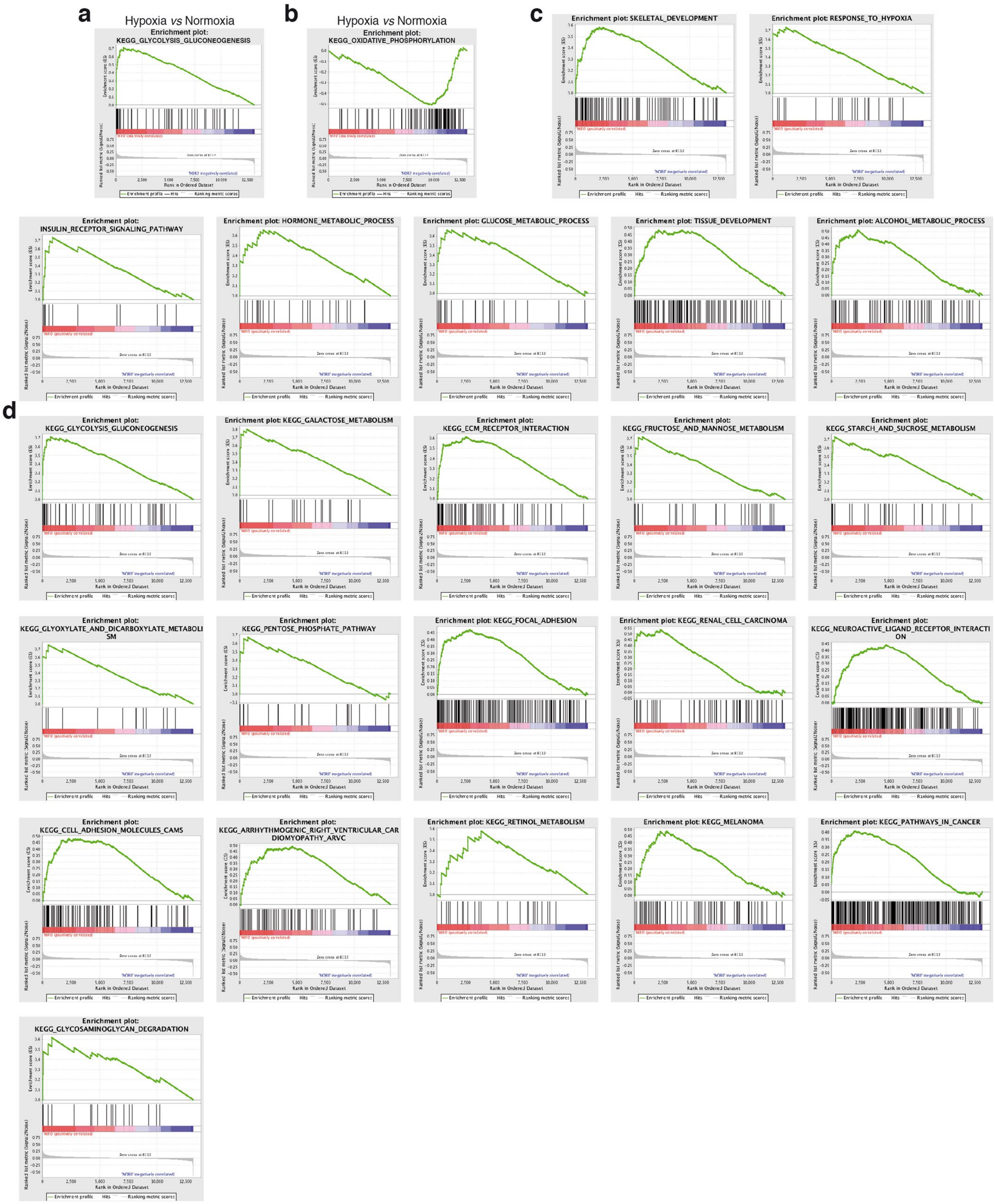

Extended Data Fig. 4 | Gene sets enriched in hypoxic primary microglial cell cultures. Enrichment plots of the GSs upregulated in hypoxic (1% O$_2$; 6 h) *versus* normoxic (1% O$_2$) primary microglial cell cultures. **a**, KEGG_GLYCOLYSIS_GLUCONEOGENESIS GS. **b**, KEGG_OXIDATIVE_PHOSPHORYLATION GS. **c**, **d**, Only significantly overrepresented GSs from biological processes (**c**) or KEGG (**d**) categories are displayed (FDR *q*-value < 0.05).

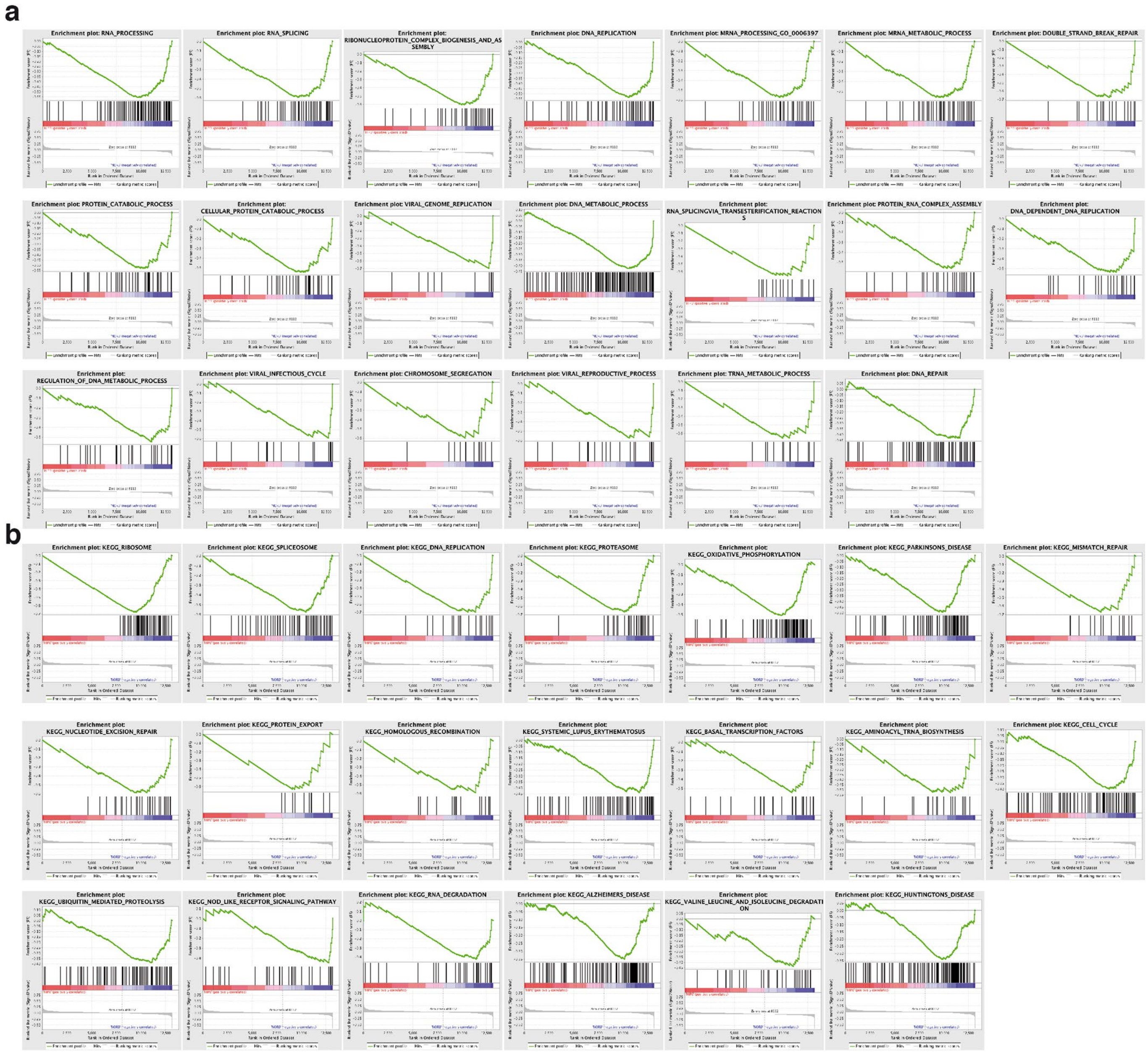

Extended Data Fig. 5 | Gene sets downregulated in hypoxic primary microglial cell cultures. Enrichment plots of the GSs downregulated in hypoxic (1% O_2; 6h) *versus* normoxic (1% O_2) primary microglial cell cultures. **a**, **b**, Only significantly overrepresented GSs from biological processes (**a**) or KEGG (**b**) categories are displayed (FDR *q*-value < 0.05).

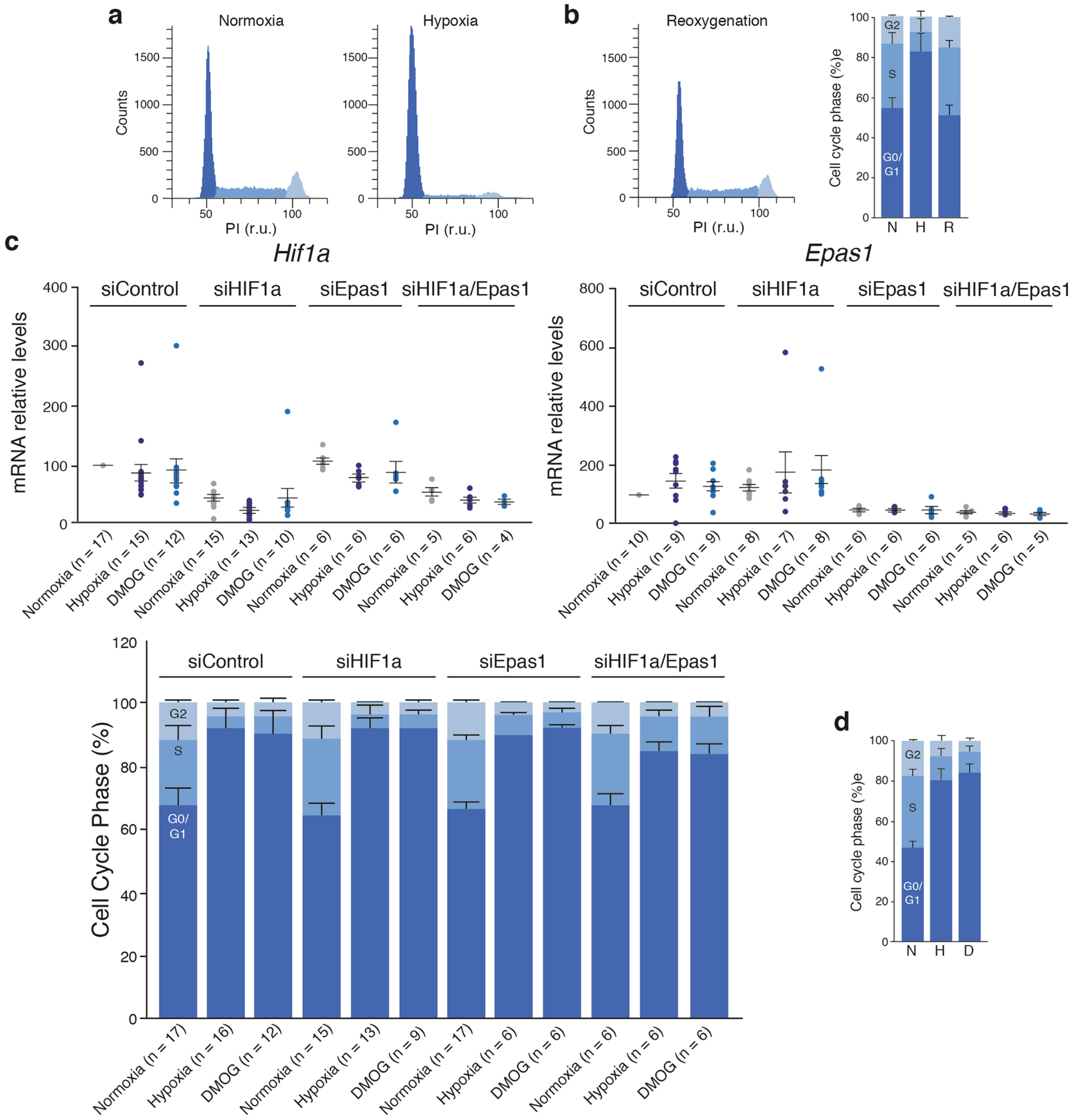

Extended Data Fig. 6 | Hypoxic cell cycle arrest in BV2 cells. a, **b**, **d**, Cell cycle analysis using propidium iodide (PI) staining of BV2 cells exposed to normoxia (N: 21% O_2, 48 h, **a**, left graph), hypoxia (H: 1% O_2, 48 h, **a**, right graph), reoxygenation (R: 24 h H and 24 h N, **b**), or DMOG (D; 0.1 mM 24 h). The quantification of the percentage of cells found in the different cell cycle phases is shown in (**b**) and (**d**) ($n = 3$ biological independent cultures). **c**, BV2 cells were treated with a scrambled siRNA (siControl) or siRNAs against *Hif1a* (siHIF1a), *Epas1* (siEpas1) and HIF1a-Epas1 (siHIF1a/Epas1). Interfered cells were exposed to N, H (24 h), or D (24 h) and the mRNA levels of *Hif1a* (left graph) and *Epas1* (right graph), and the cell cycle (lower row) were estimated by qRT-PCR (*n* is indicated between brackets, biological independent cultures). Data are represented as mean ± S.E.M.

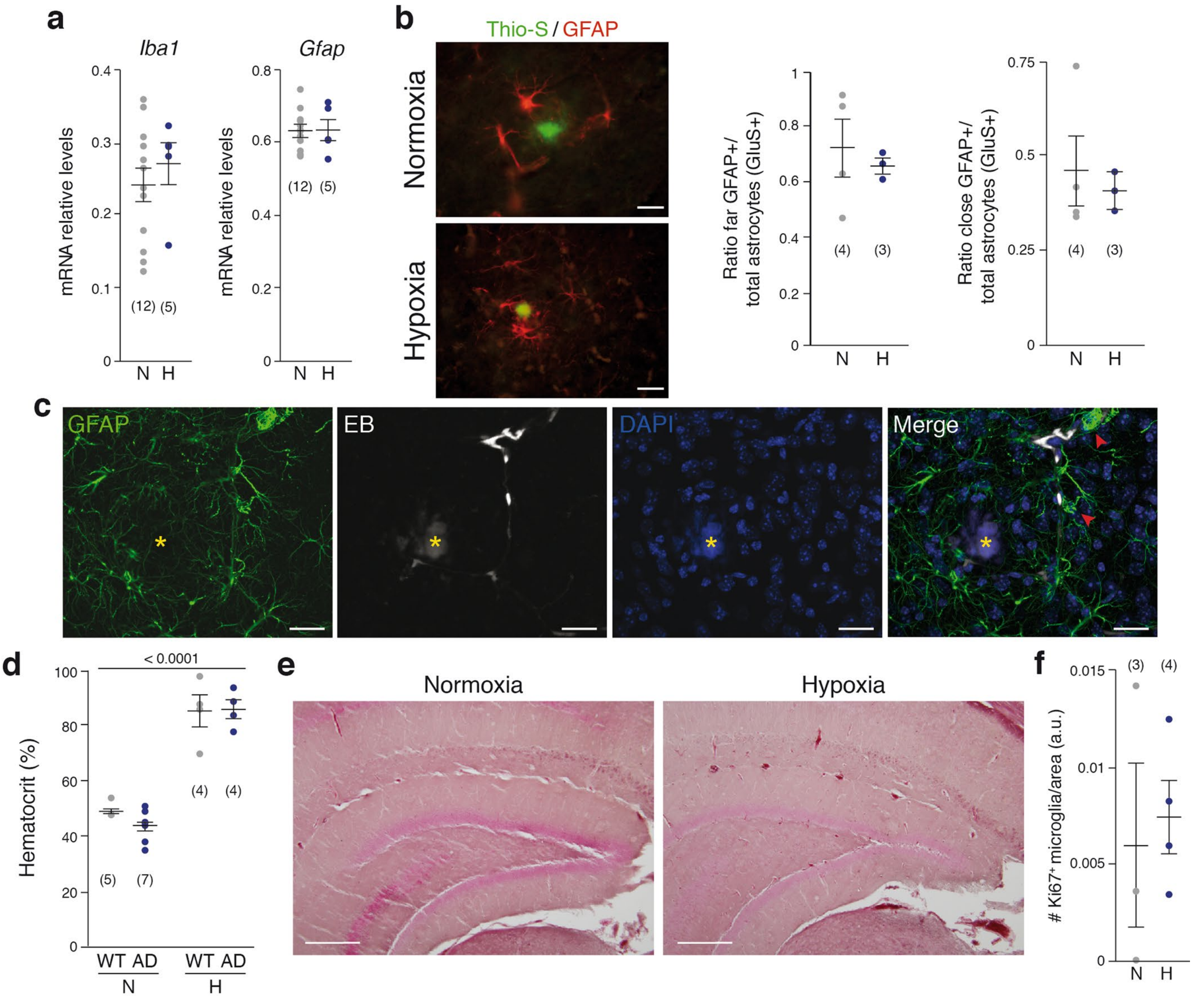

Extended Data Fig. 7 | Systemic sustained hypoxia does not alter Aß plaque-associated astrocytes or wild-type microglia. a, Relative levels of *Iba1* and *Gfap* mRNA extracted from the hippocampus of 14-month-old normoxic (N, 21% O_2) and hypoxic (H, 9% O_2) mice. *Gapdh* mRNA was used as housekeeping control (Student's *t*-test, two-sided). **b**, Cortical Aß dense-core plaques stained with Thioflavin-S (Thio-S; green) surrounded by GFAP + reactive astrocytes (red) in 14-month-old *APP-PSEN1/+* mice exposed to either N or H. Scales bar are 20 µm. Graphs show the quantification of the ratio of GFAP + astrocytes far (> 20 µm) per total astrocytes (Glutamine synthetase –GluS– immunoreactive astrocytes; left graph) and the ratio of $GFAP^+$ astrocytes close (≤ 20 µm) per total astrocytes ($GluS^+$; right graph) (ANOVA, Tukey's test). **c**, Confocal projection of coronal brain slices from 8-month-old *APP-PSEN1/+* mice injected with Evans blue (EB; white) and stained with an astrocytic (GFAP; green) and a nuclear (DAPI; blue) marker. Red arrowheads indicate reactive astrocytic endfeet. Scale bars are 20 µm. **d**, Hematocrit levels in N or H (Oxygen/Genotype: $F = 0.63$, $p = 0.336$; Oxygen: $F = 283.06$, $p = 0.000$; Univariate analysis of variance, non-adjusted for multiple correlations). **e**, Prussian blue staining of N or H. Scales bar are 100 µm. **f**, Quantification of the density of $Ki67^+$ microglial cells in N or H. (Student's *t*-test, two-sided). Data are represented as mean ± S.E.M. *n* is indicated between brackets, biological independent experiments.

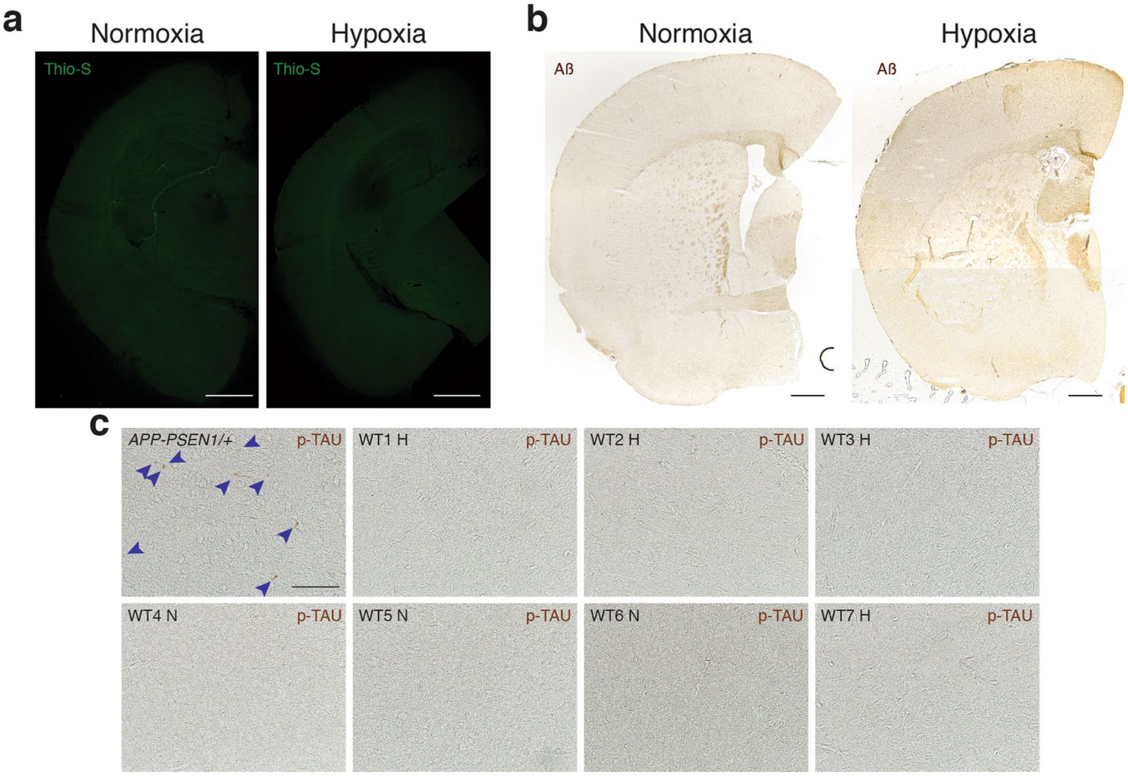

Extended Data Fig. 8 | Systemic sustained hypoxia does not induce Aß deposition in wild-type mice. a–**c**, 14-month-old wild-type mice were exposed to normoxia (N, 21% O_2) or sustained hypoxia (H, 9% O_2) for 21 days. No Thio-S (**a**), Aß (**b**) or pTAU (**c**) reactive deposits were found (*n* = 3 -N- or 4 -H- biological independent mice). Scale bars are 1 mm.

nature research

Corresponding author(s): Pascual, Alberto

Last updated by author(s): Mar 4, 2021

Reporting Summary

Nature Research wishes to improve the reproducibility of the work that we publish. This form provides structure for consistency and transparency in reporting. For further information on Nature Research policies, see our Editorial Policies and the Editorial Policy Checklist.

Statistics

For all statistical analyses, confirm that the following items are present in the figure legend, table legend, main text, or Methods section.

n/a	Confirmed	
☐	☒	The exact sample size (*n*) for each experimental group/condition, given as a discrete number and unit of measurement
☐	☒	A statement on whether measurements were taken from distinct samples or whether the same sample was measured repeatedly
☐	☒	The statistical test(s) used AND whether they are one- or two-sided *Only common tests should be described solely by name; describe more complex techniques in the Methods section.*
☐	☒	A description of all covariates tested
☐	☒	A description of any assumptions or corrections, such as tests of normality and adjustment for multiple comparisons
☐	☒	A full description of the statistical parameters including central tendency (e.g. means) or other basic estimates (e.g. regression coefficient) AND variation (e.g. standard deviation) or associated estimates of uncertainty (e.g. confidence intervals)
☐	☒	For null hypothesis testing, the test statistic (e.g. *F*, *t*, *r*) with confidence intervals, effect sizes, degrees of freedom and *P* value noted *Give P values as exact values whenever suitable.*
☒	☐	For Bayesian analysis, information on the choice of priors and Markov chain Monte Carlo settings
☒	☐	For hierarchical and complex designs, identification of the appropriate level for tests and full reporting of outcomes
☒	☐	Estimates of effect sizes (e.g. Cohen's *d*, Pearson's *r*), indicating how they were calculated

Our web collection on statistics for biologists contains articles on many of the points above.

Software and code

Policy information about availability of computer code

Data collection	Not data collection software was used
Data analysis	Fiji (v. 2.0.0) Matlab R2018a (MathWorks) GraphPad Prism version 9.0 (GraphPad Inc.) BD FACSDiva software 8.0 Olyvia 2.6 image viewer software (Olympus) Expression Console software (Affymetrix) LIMMA/Bioconductor packages (RStudio, Inc.) Visilog 6.3 (Noesis) NewCAST system (Visiopharm)

For manuscripts utilizing custom algorithms or software that are central to the research but not yet described in published literature, software must be made available to editors and reviewers. We strongly encourage code deposition in a community repository (e.g. GitHub). See the Nature Research guidelines for submitting code & software for further information.

Data

Policy information about availability of data

All manuscripts must include a data availability statement. This statement should provide the following information, where applicable:

- Accession codes, unique identifiers, or web links for publicly available datasets
- A list of figures that have associated raw data
- A description of any restrictions on data availability

The raw data are available at the Source Data accompanying this article. Transcriptomics data are available at GEO with the following accession numbers: (i) Mouse primary microglial cultures exposed to normoxia or hypoxia: GSE97423; (ii) Isolated Clec7a+ microglia from WT, APP751SL and MAPTp.P301S mice: GSE129296; and (iii) Isolated microglia from APP-PSEN1/+; VHLFlox/– with or without TMX treatment GSE168059.

Field-specific reporting

Please select the one below that is the best fit for your research. If you are not sure, read the appropriate sections before making your selection.

☒ Life sciences ☐ Behavioural & social sciences ☐ Ecological, evolutionary & environmental sciences

For a reference copy of the document with all sections, see nature.com/documents/nr-reporting-summary-flat.pdf

Life sciences study design

All studies must disclose on these points even when the disclosure is negative.

Sample size	No sample calculations were performed. The number used was selected based in previous publications in the field.
Data exclusions	No data were excluded
Replication	All the experiments were replicated in biological samples and no repetition was excluded from the study. All replication attempts were successful. A minimum of three replications was performed.
Randomization	Allocation was random
Blinding	All quantifications were done blinded (see M&M section).

Reporting for specific materials, systems and methods

We require information from authors about some types of materials, experimental systems and methods used in many studies. Here, indicate whether each material, system or method listed is relevant to your study. If you are not sure if a list item applies to your research, read the appropriate section before selecting a response.

Materials & experimental systems

n/a	Involved in the study	
☐	☒	Antibodies
☐	☒	Eukaryotic cell lines
☒	☐	Palaeontology and archaeology
☐	☒	Animals and other organisms
☐	☒	Human research participants
☒	☐	Clinical data
☒	☐	Dual use research of concern

Methods

n/a	Involved in the study	
☒	☐	ChIP-seq
☐	☒	Flow cytometry
☒	☐	MRI-based neuroimaging

Antibodies

Antibodies used

Alexa-488 and Alexa-568-conjugated streptavidin, Jackson, 1:500.
Alexa-488, Alexa-568, and Alexa-647, Molecular Probes, 1:800
anti-Aß 6e10 (Biolegend, 1:500)
anti-Aß antibody (Biolegend, anti-Aβ17-24, clone 4G8, 1:2,000,)
anti-ATPsynß (BD, 1:1000, 612519)
anti-BrdU primary antibody (Abcam, 1:250, Ab6326)
anti-CD11b-APC, eBioscience, 1:200
anti-CD11b-CFblue (M1/70, Immunostep) 5:100
anti-CD16/CD32, eBioscience, 1:200
anti-CD45-PE (M45PE, Immunostep) 3:100
anti-CD45-PE, eBioscience, 1:200

anti-CLEC7a-FITC (FAB14561Gm, R&D Systems) 15:100
anti-CLEC7a-FMO, Fluorescence Minus One
anti-GFAP Sigma, 1:1,000 G3893
anti-GS (Millipore, 1:1,000)
anti-HIF1alpha (Cayman, 1:100; 10006421)
anti-IBA1, Wako, 1:400 01-1974
anti-Ki67 (BD, 1:200, 550609)
anti-mouse (GE Healthcare, 1:10,000; NA931)
anti-NDUFS2 (AbCam, 1:1000, ab103024)
anti-RPL26 (SIGMA, 1:1000, R0655)
anti-ß-actin (Abcam, 1:5,000; ab6276)
anti-SDHD (AbCam, 1:1000, ab14715)
anti-UB (DAKO, 1:400)
control-PE (e-Bioscience; 1:200)
HRP-conjugated anti-rabbit (Thermo, 1:10,000; 31460)
Isotype control-APC (eBioscience; 1:200)
p-Tau –AT8–, Thermo, 1:500

Validation

anti-Aß 6e10 (Biolegend, 1:500). Ref. 7 in the main text, mouse and human.
anti-Aß antibody (Biolegend, anti-Aβ17-24, clone 4G8, 1:2,000,). Ref. 7 in the main text, mouse and human.
anti-ATPsynß (BD, 1:1000, 612519)
1. Lee JH, Garboczi DN, Thomas PJ, Pedersen PL. Mitochondrial ATP synthase. cDNA cloning, amino acid sequence, overexpression, and properties of the rat liver alpha subunit. J Biol Chem. 1990; 265(8):4664-4669. View reference
2. Ohta S, Tomura H, Matsuda K, Kagawa Y. Gene structure of the human mitochondrial adenosine triphosphate synthase beta subunit. J Biol Chem. 1988; 263(23):11257-11262. View reference
3. Villena JA, Martin I, Vinas O, et al. ETS transcription factors regulate the expression of the gene for the human mitochondrial ATP synthase beta-subunit. J Biol Chem. 1994; 269(51):32649-32654. View reference
anti-BrdU primary antibody (Abcam, 1:250, Ab6326)
https://www.abcam.com/brdu-antibody-bu175-icr1-proliferation-marker-ab6326.html
1165 publications, mouse
anti-CD11b-APC, eBioscience, 1:200
1. Ault KA, Springer TA. Cross-reaction of a rat-anti-mouse phagocyte-specific monoclonal antibody (anti-Mac-1) with human monocytes and natural killer cells. J Immunol. 1981; 126(1):359-364. View reference
2. Beller DI, Springer TA, Schreiber RD. Anti-Mac-1 selectively inhibits the mouse and human type three complement receptor. J Exp Med. 1982; 156(4):1000-1009. View reference
3. Kishimoto TK, Jutila MA, Berg EL, Butcher EC. Neutrophil Mac-1 and MEL-14 adhesion proteins inversely regulated by chemotactic factors. Science. 1989; 245(4923):1238-1241. View reference
4. Lagasse E, Weissman IL. Flow cytometric identification of murine neutrophils and monocytes. J Immunol Methods. 1996; 197(1-2):139-150. View reference
5. Lub M, van Kooyk Y, Figdor CG. Competition between lymphocyte function-associated antigen 1 (CD11a/CD18) and Mac-1 (CD11b/CD18) for binding to intercellular adhesion molecule-1 (CD54). J Leukoc Biol. 1996; 59(5):648-655. View reference
6. Sanchez-Madrid F, Simon P, Thompson S, Springer TA. Mapping of antigenic and functional epitopes on the alpha- and beta-subunits of two related mouse glycoproteins involved in cell interactions, LFA-1 and Mac-1. J Exp Med. 1983; 158(2):586-602. View reference
7. Springer T, Galfre G, Secher DS, Milstein C. Mac-1: a macrophage differentiation antigen identified by monoclonal antibody. Eur J Immunol. 1979; 9(4):301-306. View reference
8. Springer T, Galfre G, Secher DS, Milstein C. Monoclonal xenogeneic antibodies to murine cell surface antigens: identification of novel leukocyte differentiation antigens. Eur J Immunol. 1978; 8(8):539-551. View reference
9. Springer TA, Davignon D, Ho MK, Kurzinger K, Martz E, Sanchez-Madrid F. LFA-1 and Lyt-2,3, molecules associated with T lymphocyte-mediated killing; and Mac-1, an LFA-1 homologue associated with complement receptor function. Immunol Rev. 1982; 68:171-195. View reference
anti-CD11b-CFblue (M1/70, Immunostep) 5:100
Ault KA, Springer TA. Cross-reaction of a ratanti-mouse phagocyte-specific monoclonal antibody (anti-Mac-1) with human monocytes and natural killer cells. J Immunol1981 Jan;126(1):359-64. 2. Dembic Z, Schenck K, Bogen B. Dendritic cells purified from myeloma are primed with tumorspecific antigen (idiotype) and activate CD4+ T cells. Proc Natl Acad Sci U S A2000 Mar 14;97(6):2697-702. 3. Sanchez-Madrid F, Simon P, Thompson S, Springer TA. Mapping of antigenic and functional epitopes on the alpha- and betasubunits of two related mouse glycoproteins involved in cell interactions, LFA-1 and Mac-1. J Exp Med1983 Aug 1;158(2):586-602. 4. Springer T, Galfre G, Secher DS, Milstein C. Monoclonal xenogeneic antibodies to murine cell surface antigens: identification of novel leukocyte differentiation antigens. Eur J Immunol1978 Aug;8(8):539-51. 5. Springer T, Galfre G, Secher DS, Milstein C. Mac1: a macrophage differentiation antigen identified by monoclonal antibody. Eur J Immunol1979 Apr;9(4):301-6. 6. Zhang Y, McCormick LL, Desai SR, Wu C, Gilliam AC. Murine sclerodermatous graftversus-host disease, a model for human scleroderma: cutaneous cytokines, chemokines, and immune cell activation. J Immunol2002 Mar 15;168(6):3088-98.
anti-CD16/CD32, eBioscience, 1:200
Nature communications
miR-143/145 differentially regulate hematopoietic stem and progenitor activity through suppression of canonical TGFβ signaling.
"Published figure using CD16/CD32 monoclonal antibody (Product # 48-0161-82) in Flow Cytometry"
anti-CD45-PE (M45PE, Immunostep) 3:100
Pulido R, Cebrian M, Acevedo A, de Landazuri MO, Sanchez-Madrid F. Comparative biochemical and tissue distribution study of four distinct CD45 antigen specificities. J Immunol1988 Jun 01;140(11):3851-7. 2. Cyster JG, Healy JI, Kishihara K, Mak TW, Thomas ML, Goodnow CC. Regulation of Blymphocyte negative and positive selection by tyrosine phosphatase CD45. Nature1996 May 23;381(6580):325-8. 3. Leitenberg D, Novak TJ, Farber D, Smith BR, Bottomly K. The extracellular domain of CD45 controls association with the CD4-T cell receptor complex and the response to antigen-specific stimulation. J Exp Med1996 Jan 01;183(1):249-59.
anti-CD45-PE, eBioscience, 1:200
Oncoimmunology
The Interleukin (IL)-1R1 pathway is a critical negative regulator of PyMT-mediated mammary tumorigenesis and pulmonary

metastasis.
"Published figure using CD45 monoclonal antibody (Product # 12-0451-82) in Flow Cytometry"
anti-CLEC7a-FITC (FAB14561Gm, R&D Systems) 15:100
Front. Cell. Neurosci., 14 November 2018 | https://doi.org/10.3389/fncel.2018.00421
anti-CLEC7a-FMO, Fluorescence Minus One
Front. Cell. Neurosci., 14 November 2018 | https://doi.org/10.3389/fncel.2018.00421
anti-GFAP Sigma, 1:1,000 G3893
Ref. 7 in the main text, mouse and human.
anti-GS (Millipore, 1:1,000)
Ref. 7 in the main text, mouse and human.
anti-HIF1alpha (Cayman, 1:100; 10006421)
The Journal of Biological Chemistry, 03 Feb 2012, 287(12):9651-9658 Mouse and Human
DOI: 10.1074/jbc.m111.299180
anti-IBA1, Wako, 1:400 01-1974
Ref. 7 in the main text, mouse and human
anti-Ki67 (BD, 1:200, 550609)
Ref. 7 in the main text, mouse and human
anti-NDUFS2 (AbCam, 1:1000, ab103024)
Cell metabolism Volume 22, Issue 5, 3 November 2015, Pages 825-837
anti-RPL26 (SIGMA, 1:1000, R0655)
The Journal of Biological Chemistry, 03 Feb 2012, 287(12):9651-9658 Mouse
DOI: 10.1074/jbc.m111.299180
anti-ß-actin (Abcam, 1:5,000; ab6276)
The Journal of Biological Chemistry, 03 Feb 2012, 287(12):9651-9658 Mouse
DOI: 10.1074/jbc.m111.299180
anti-SDHD (AbCam, 1:1000, ab14715)
Cell metabolism Volume 22, Issue 5, 3 November 2015, Pages 825-837
anti-UB (DAKO, 1:400)
Ref. 7 in the main text, mouse and human
p-Tau –AT8–, Thermo, 1:500
Ref. 7 in the main text, mouse and human

Eukaryotic cell lines

Policy information about cell lines

Cell line source(s)	Interlab Cell Line Collection (ICLC) (BV2) and ATTC (HeLa)
Authentication	Non-authenticated
Mycoplasma contamination	Negative
Commonly misidentified lines (See ICLAC register)	The cell lines used were no commonly misidentified

Animals and other organisms

Policy information about studies involving animals; ARRIVE guidelines recommended for reporting animal research

Laboratory animals	Mouse, both sexes, C57/Bl6J and mixed background. Mice were housed under controlled temperature (22ºC) and humidity conditions in a 12 h light/dark cycle with ad libitum access to food and water. Ages between 2 and 14-month-old.
Wild animals	No wild mice were used
Field-collected samples	No field-collected samples were used
Ethics oversight	Housing and treatments were performed according to the animal care guidelines of European Community Council (86/60/EEC). Principles of laboratory animal care (NIH publication No. 86-23, revised 1985) were followed, as well as specific Spanish national laws where applicable. The competent Spanish authority approved all the procedures ("Consejería de agricultura, pesca y desarrollo rural. Dirección general de la producción agrícola y ganadera"). All animal procedures were conformed under the Spanish law and approved with number 26/04/2016/064 ("Consejería de agricultura, pesca y desarrollo rural. Dirección general de la producción agrícola y ganadera").

Note that full information on the approval of the study protocol must also be provided in the manuscript.

Human research participants

Policy information about studies involving human research participants

Population characteristics	Autopsy samples were obtained from the Neurological Tissue Bank of IDIBELL-Hospital of Bellvitge (Barcelona, Spain). The study (CEEA-US2017-13) was approved by the local ethics committee and by the "Comite de Etica de la Investigación (CEI), Hospital Virgen del Rocío", Seville, Spain. Samples with signed informed consent from "Banco de tejidos: Fundación CIEN (BT-

CIEN; Centro de Investigación de Enfermedades Neurologicas; Madrid, Spain)" and from the Neurological Tissue Bank of IDIBELL-Hospital of Bellvitge (Barcelona, Spain), classified by Braak tau pathology (Supplementary Table 12):
Human samples
Sex (% female) Sex (% male) Age PMD delay
Braak 0 37.5 62.5 49.5 ± 5.9 7.2 ± 3.3
AD II 61.54 38.46 78 ± 8.5 8.3 ± 5.3
AD III/IV 55.6 44.4 78.3 ± 14.0 5.8 ± 5.0
AD V/VI 38.89 61.11 79 ± 10.0 7.5 ± 3.7

Recruitment

Describe how participants were recruited. Outline any potential self-selection bias or other biases that may be present and how these are likely to impact results.

Ethics oversight

Identify the organization(s) that approved the study protocol.

Note that full information on the approval of the study protocol must also be provided in the manuscript.

Flow Cytometry

Plots

Confirm that:

☒ The axis labels state the marker and fluorochrome used (e.g. CD4-FITC).

☒ The axis scales are clearly visible. Include numbers along axes only for bottom left plot of group (a 'group' is an analysis of identical markers).

☒ All plots are contour plots with outliers or pseudocolor plots.

☒ A numerical value for number of cells or percentage (with statistics) is provided.

Methodology

Sample preparation

Microglial cells isolation method was as described (12). Briefly, mice were anesthetised and transcardially perfused with HBSS (–CaCl2/–MgCl2) (Gibco) and cortices were dissected and then dissociated using a Tissue Chopper (Vibratome, 800 series). Chemical digestion was then performed with a mix of papain (Worthington) (8 U/mL) and DNAse I (SIGMA; 80 Kunitz units/mL) followed by a Percoll gradient (GE healthcare) at 90 % in PBS (v/v). Cells were stained with primary conjugated monoclonal antibodies CD11b-APC (eBioscience) and CD45-PE (BD Bioscience) diluted 1:200 at 4°C for 30 min. Staining with isotype control-PE and isotype control-APC (eBioscience) at 1:200 dilution was used as negative control. Both control and experimental samples were simultaneously incubated with anti-CD16/CD32 (e-Bioscience) blocker antibody at 1:200. Cells were washed and sorted using a FACS Aria Fusion (Becton Dickinson) flow cytometer and data
acquired and analysed with FACSDiva software 8.0 (Becton Dickinson).
To separate CLEC7a high and low populations, we used an anti-CD45-PE (M45PE, Immunostep) 3:100 v/v and an anti-CD11b-CFblue (M1/70, Immunostep) 5:100 v/v, combined with an anti-CLEC7a-FITC (FAB14561Gm, R&D Systems) 15:100 v/v at RT for 20 min. An anti-CLEC7a-FMO (Fluorescence Minus One) control was included (cells stained with anti-CD45-PE and anti-CD11b-CFblue, but not with anti-CLEC7a-FITC) in order to stablish autofluorescence values in the FITC channel.

Instrument

FACS Aria Fusion (Becton Dickinson)

Software

FACSDiva software 8.0 (Becton Dickinson)

Cell population abundance

Purity was determined by qRT-PCR of sorted cells using several markers.

Gating strategy

Gating strategy and data analysis was made according to guidelines. (ref. 53 in the text). Isolated cells were stained with antibodies CD11b-APC and CD45-PE at 4°C for 30 min. Staining with isotype control-PE and isotype control-APC was used as a negative control. Both control and experimental samples were incubated with anti-CD16/CD32 blocker simultaneously. Cells were washed and sorted using a FACS Aria Fusion (Becton Dickinson) flow cytometer and data were acquired and analyzed with FACSDiva software 8.0 (Becton Dickinson). Gating strategy and data analysis were made according to guidelines 1. To separate CLEC7a high and low populations, we used an anti-CD45-PE and an anti-CD11b-CFblue, with an anti-CLEC7a-FITC at RT for 20 min. Anti-CLEC7a-FMO control was included (cells stained with anti-CD45-PE and anti-CD11b-CFblue, but not with anti-CLEC7a-FITC) for autofluorescence values in the FITC channel.

☒ Tick this box to confirm that a figure exemplifying the gating strategy is provided in the Supplementary Information.